




RESEARCH ARTICLE

Assessing methods for geometric distortion compensation in 7 T gradient echo functional MRI data

Michael-Paul Schallmo¹  | Kimberly B. Weldon^{2,1}  | Philip C. Burton^{3,2} |
Scott R. Sponheim^{4,1} | Cheryl A. Olman^{5,2} 

¹Department of Psychiatry and Behavioral Sciences, University of Minnesota, Minneapolis, Minnesota

²Center for Magnetic Resonance Research, University of Minnesota, Minneapolis, Minnesota

³Office of the College of Liberal Arts Associate Dean for Research, University of Minnesota, Minneapolis, Minnesota

⁴Veterans Affairs Medical Center, Minneapolis, Minnesota

⁵Department of Psychology, University of Minnesota, Minneapolis, Minnesota

Correspondence

Michael-Paul Schallmo, Department of Psychiatry and Behavioral Sciences, University of Minnesota, Minneapolis, MN.
Email: schal110@umn.edu

Funding information

National Center for Advancing Translational Sciences, Grant/Award Number: UL1 TR002494; National Institute of Biomedical Imaging and Bioengineering, Grant/Award Number: P41 EB015894; National Institute of Mental Health, Grant/Award Numbers: K01 MH120278, R01 MH111447, U01 MH108150; National Institute of Neurological Disorders and Stroke, Grant/Award Number: P30 NS076408

Abstract

Echo planar imaging (EPI) is widely used in functional and diffusion-weighted MRI, but suffers from significant geometric distortions in the phase encoding direction caused by inhomogeneities in the static magnetic field (B_0). This is a particular challenge for EPI at very high field (≥ 7 T), as distortion increases with higher field strength. A number of techniques for distortion correction exist, including those based on B_0 field mapping and acquiring EPI scans with opposite phase encoding directions. However, few quantitative comparisons of distortion compensation methods have been performed using human EPI data, especially at very high field. Here, we compared distortion compensation using B_0 field maps and opposite phase encoding scans in two different software packages (FSL and AFNI) applied to 7 T gradient echo (GE) EPI data from 31 human participants. We assessed distortion compensation quality by quantifying alignment to anatomical reference scans using Dice coefficients and mutual information. Performance between FSL and AFNI was equivalent. In our whole-brain analyses, we found superior distortion compensation using GE scans with opposite phase encoding directions, versus B_0 field maps or spin echo (SE) opposite phase encoding scans. However, SE performed better when analyses were limited to ventromedial prefrontal cortex, a region with substantial dropout. Matching the type of opposite phase encoding scans to the EPI data being corrected (e.g., SE-to-SE) also yielded better distortion correction. While the ideal distortion compensation approach likely varies depending on methodological differences across experiments, this study provides a framework for quantitative comparison of different distortion compensation methods.

KEYWORDS

7 Tesla, B_0 inhomogeneity, distortion compensation, echo planar imaging, field map, functional MRI

1 | INTRODUCTION

Geometric fidelity is critical for high quality brain imaging. It is essential for accurate interpretation of functional MRI (fMRI) data based on anatomical landmarks and is necessary for precise quantification of structural and functional connectivity. It is also relevant for clinical brain imaging applications, such as neurosurgery and the placement of deep brain stimulation electrodes (Menuel et al., 2005; Sumanaweera et al., 1995; Sumanaweera, Glover, Binford, & Adler, 1993). However, currently popular MRI techniques suffer from a number of common artifacts that degrade spatial fidelity, including gradient nonlinearities and geometric distortion due to static magnetic field (B_0) inhomogeneity (Bakker, Moerland, Bhawandien, & Beersma, 1992; Jezzard & Clare, 1999). A number of methods to correct for these geometric artifacts have been established (Bakker et al., 1992; Esteban et al., 2014; Gholipour, Kehtarnavaz, Scherrer, & Warfield, 2011; Graham, Drobnyak, Jenkinson, & Zhang, 2017; Holland, Kuperman, & Dale, 2010; Hong, To, Teh, Soh, & Chuang, 2015; Hutton et al., 2002; Jezzard & Clare, 1999; Wang et al., 2017). To select an appropriate method for distortion correction, quantitative comparisons between methods are essential.

Echo planar imaging (EPI) is among the most commonly used MRI techniques in human neuroscience. Rapid acquisition times enable studies of functional brain activation (i.e., fMRI; often ≤ 1 s per whole-brain image) and efficient measurement of white matter tractography via diffusion-weighted MRI (dMRI; on the order of 5 s per image). This temporal efficiency comes at the cost of relatively low pixel bandwidth in the phase encoding (PE) direction, which results in severe geometric distortions in regions of B_0 inhomogeneity (Gholipour et al., 2011; Hutton et al., 2002; Jezzard & Clare, 1999). Lower bandwidth (i.e., longer effective echo spacing) makes distortion more severe; distortion of some regions in EPI data in the PE direction often reaches 5–10 mm (Jezzard & Clare, 1999). B_0 inhomogeneities and the resulting distortions are greatest at the interface of different tissue types (e.g., brain, bone, air) in regions such as the orbitofrontal cortex and temporal lobes. Inhomogeneities also scale linearly with B_0 field strength, such that geometric distortions can be more severe at 7 Tesla than at 3 Tesla (Dymerska, Poser, Barth, Tractnig, & Robinson, 2018).

A number of methods for minimizing and correcting geometric distortion in EPI data exist. Prospectively, geometric distortion can be limited by reducing B_0 inhomogeneity via B_0 shimming, and confirming shim quality during a scan by measuring the linewidth of the water signal. Geometric distortion can also be limited by shortening read-out time. Methods for this include: (1) using multishot or segmented EPI (Feinberg & Oshio, 1994; McKinnon, 1993; Moeller, Van de Moortele, Goerke, Adriany, & Ugurbil, 2006) (rather than single-shot sequences, at the cost of longer TRs and increased physiological noise sensitivity), (2) using a higher parallel imaging acceleration factor (R; at the cost of reduced signal-to-noise ratio [SNR]), (3) increasing receiver bandwidth (e.g., reducing echo spacing, or using stronger or faster head gradients, at the cost of reduced SNR), (4) decreasing the field of view in the PE direction (at the cost of reduced spatial coverage) (Olman, Davachi, & Inati, 2009). Although one might be tempted

to think that distortion would also be attenuated by reducing the sampling of k -space data in the PE direction using partial Fourier approaches, this is not the case because partial Fourier does not change the pixel bandwidth. Finally, it is worth noting that when using spiral acquisition sequences (Glover & Law, 2001) in place of EPI, B_0 inhomogeneity produces blurring rather than geometric distortion, which may be preferable for some applications that do not require high spatial specificity.

It is also possible to correct geometric distortion in an EPI dataset retrospectively, which has been shown to improve registration between EPI and T_1 -weighted anatomical data (Hutton et al., 2002). A number of different methods for retrospective distortion compensation have been introduced, including:

1. B_0 field mapping by measuring phase differences from two gradient echo (GE) images with different echo times (TEs) (Hunsche et al., 2004; Hutton et al., 2002; Jezzard & Balaban, 1995),
2. calculating a distortion field based on two EPI scans with opposite PE directions (i.e., forward & reverse, often anterior–posterior (AP) and posterior–anterior (PA); hereafter, referred to as opposite PE [oppPE] field mapping), for which the geometric distortion will be equal but in opposite directions (Andersson, Skare, & Ashburner, 2003; Embleton, Haroon, Morris, Ralph, & Parker, 2010; Morgan, Bowtell, McIntyre, & Worthington, 2004),
3. nonrigid registration (e.g., affine or spline fitting) of the distorted EPI to a minimally distorted anatomical reference (Gholipour et al., 2006; Li et al., 2006; Li et al., 2007; Li, Xu, Fitzpatrick, & Dawant, 2008; Studholme, Constable, & Duncan, 2000),
4. mapping the EPI point-spread function (In, Posnansky, & Speck, 2017; Robson, Gore, & Constable, 1997; Zaitsev, Hennig, & Speck, 2004; Zeng & Constable, 2002),
5. methods based on forward and inverse modeling of the distortion (Andersson, Hutton, Ashburner, Turner, & Friston, 2001; Munger, Crelier, Peters, & Pike, 2000),
6. multireference scan methods (Wan, Gullberg, Parker, & Zeng, 1997),
7. hybrid methods (e.g., B_0 or oppPE field mapping plus nonrigid registration) (Gholipour et al., 2011; Hong et al., 2015; Hunsche et al., 2004), and
8. dynamic methods for correcting time-varying geometric distortions due to factors such as head movement (Andersson et al., 2001; Barry et al., 2010; Dymerska et al., 2018).

Of these, the first two (B_0 and oppPE field maps) are arguably the most popular and are currently implemented in various forms across many widely used MRI analysis software packages (e.g., FSL (Smith et al., 2004), AFNI (Cox, 1996), SPM (Friston et al., 1994), BrainVoyager (Goebel, Esposito, & Formisano, 2006)). Thus, we chose to focus on quantitative comparisons between B_0 and oppPE field map approaches in the current study.

With regard to oppPE field maps, it has been suggested that spin echo (SE) EPI scans may offer an advantage over GE sequences in mapping the distortion field (Holland et al., 2010), as the former

minimizes signal dropout from through-slice dephasing due to the 180° refocusing pulse at $TE/2$. This suggests that a pair of SE EPI scans with opposite PE directions should give a more complete map of field inhomogeneities than a GE oppPE pair. However, this theoretical motivation has not, to our knowledge, been tested empirically. Alternatively, one may consider whether other factors could limit the utility of SE oppPE field maps for the correction of geometric distortion in GE EPI data. For example, there may be increased opportunity for subject motion due to added scan time, as two additional SE scans must be acquired (forward and reverse PE) versus only one additional GE scan (reverse) to correct GE EPI data (which itself can serve as the forward image in the GE oppPE pair). Further, when using SE oppPE field maps to correct distortion in GE data, image contrast differences between SE and GE could lead to incorrect mapping of voxel shifts in regions of local signal compression (Embleton et al., 2010; Graham et al., 2017). Thus, in the current study, we sought to directly and quantitatively compare the performance of different distortion compensation methods that are currently standard in the field, to explore which method would perform best in our GE fMRI dataset, and whether we might find empirical evidence for the theorized superiority of SE oppPE methods (Holland et al., 2010).

Previous studies that have compared different methods for geometric distortion compensation have generally focused on data collected at field strengths of 1.5–3 T, for which geometric distortion may be less extreme as compared to very high field (≥ 7 T). The proliferation of very high field imaging methods (Olman & Yacoub, 2011), due in part to efforts such as the Human Connectome Project (HCP; Van Essen et al., 2013; Vu et al., 2015; Glasser et al., 2016; Vu et al., 2017; Benson et al., 2018), makes it increasingly important to achieve effective geometric distortion compensation of high field EPI data. Therefore, in the current study we examined this issue using 7 T EPI data that we have collected as part of the Psychosis HCP at the University of Minnesota's Center for Magnetic Resonance Research.

Prior investigations of geometric distortion compensation methods have not, generally, included correction for additional gradient nonlinearities (Glasser et al., 2013). Gradient nonlinearities are unrelated to distortion due to B_0 inhomogeneity, are present in all three dimensions (PE, readout, and through-slice), and are sequence independent (Bakker et al., 1992). These gradient nonlinearities can be on the order of 1–2% (Bakker et al., 1992; Jezzard & Clare, 1999) and will vary between scanners due to differences in gradient hardware. Distortions due to gradient nonlinearities may therefore confound efforts to achieve high spatial fidelity in EPI data, and are particularly important to consider when trying to unify datasets acquired on different scanners (e.g., a T_1 anatomy acquired at 3 T, and GE EPI fMRI data acquired at 7 T, as in the current study) or during different scanning sessions.

In this study, we compared the methods noted above (i.e., GE and SE oppPE as well as B_0 field maps) for the correction of geometric distortion due to B_0 inhomogeneity in GE EPI data collected at very high field (7 T), following a separate initial step to correct for distortion due to known gradient nonlinearities. We sought to answer the following question: which current standard distortion compensation method(s)

would perform best for our 7 T GE fMRI data? This study presents a framework within which to answer this question for a given dataset. We do not intend to prescribe one method as definitively superior over another in all cases, as relative performance is expected to depend on acquisition parameters, order and timing of the acquisition of EPI and field map scans, scanner and radiofrequency coil hardware, the brain regions being examined, and the details of the processing pipeline that is used. Our results suggest that all of the examined methods improved correspondence between GE EPI and T_1 anatomical data, with the best performance across the whole brain being observed for GE oppPE field map methods in our dataset.

2 | METHODS

2.1 | Participants

We recruited 31 participants for the current study from a larger sample as part of the Psychosis HCP. This included 12 patients with a diagnosed psychotic disorder (e.g., schizophrenia), 9 first-degree biological relatives of patients with psychosis (i.e., parents, siblings, or children), and 10 healthy controls. Group differences were not examined in this particular study, as a subject's mental health status was not deemed relevant to the assessment of geometric distortion compensation methods. We chose to study a diverse population (i.e., including patients and controls, not expert MRI subjects) in order to make our results more broadly applicable to the type of MRI data that would be obtained in clinical populations such as adults with psychosis. Subject demographics were as follows: 20 female and 11 male participants, mean age was 45 years ($SD = 11$ years).

Inclusion criteria for the Psychosis HCP were as follows: age 18–65 years, English as primary language, the ability to provide informed consent, no legal guardian, no alcohol or drug abuse within the last 2 weeks, no alcohol or drug dependence within the last 6 months, no diagnosed learning disability or IQ less than 70, no current or past central nervous system disease, no history of head injury with skull fracture or loss of consciousness longer than 30 min, no electroconvulsive therapy within the last year, no tardive dyskinesia, no visual or hearing impairment, no condition that would inhibit task performance such as paralysis or severe arthritis. All patients had a history of bipolar I, schizophrenia, or schizoaffective disorder and were not adopted. Relatives had a biological parent, sibling, or child with a history of one of these disorders and were not adopted. Controls had no personal or family history (parents, siblings, children) of these disorders. Additional inclusion criteria for this particular study included the ability to fit comfortably within the scanner bore (60 cm diameter) and the radio frequency head coil (head circumference less than 62 cm), weight less than 440 pounds, and corrected Snellen visual acuity of 20/40 or better. Further, all participants had completed two 3 T fMRI scanning sessions prior to 7 T scanning and did not exceed a limit of 0.5 mm of head motion across greater than 20% of TRs from all 3 T fMRI runs (approximately 2 hr of scanning). Finally, participants included in this study had all 7 T MRI scans acquired in the prescribed

order (see below) and did not exceed a limit of 0.5 mm of head motion on greater than 20% of TRs during 7 T fMRI scans (1.25 hr of scanning).

All participants provided written informed consent prior to participation and were compensated for their time. All experimental procedures complied with the regulations for research on human subjects described in the Declaration of Helsinki and were approved by the Institutional Review Board at the University of Minnesota. All subjects were found to have sufficient capacity to provide informed consent, as assessed by the University of California Brief Assessment of Capacity to Consent (Jeste et al., 2007).

2.2 | Experimental protocol

7 T MRI data were acquired on a Siemens MAGNETOM scanner (software version: VB17). This scanner was equipped with an 8-kW radio frequency power amplifier and body gradients with 70 mT/m maximum amplitude and 200 T/m/s maximum slew rate. We used a Nova Medical (Wilmington, MA) radio frequency head coil with 1 transmit and 32 receive channels for all 7 T MRI data acquisition. Subjects were provided with head padding inside the coil and instructed to minimize head movements during scanning. We placed 5 mm thick dielectric pads (3:1 calcium titanate powder in water) under the neck and beside the temples, as this has been shown to improve transmit B_1 homogeneity in the cerebellum and temporal lobe regions during 7 T MRI (Vu et al., 2015).

MRI data were acquired using sequences and scan parameters that followed the original Young Adult HCP (Benson et al., 2018; Glasser et al., 2016; Van Essen et al., 2013; Vu et al., 2015; Vu et al., 2017). Parameters for the different MR scans are listed in Table 1. Additional scan parameters include a multiband acceleration factor of 5 for GE and SE fMRI, and GRAPPA parallel imaging acceleration factor (R) of 2 for all scans except the B_0 field map (no acceleration). The delta TE for the B_0 field map scan was 1.02 ms. Single-band reference scans

were acquired with each multiband EPI scan (GE and SE). Data were acquired with an oblique-axial orientation using Siemens Auto Align to standardize the orientation and positioning of the imaging field of view.

7 T MRI data in this study were acquired in a fixed scan order:

1. auto-align scout and localizer,
2. GE EPI with PA PE direction (3 TRs; Figure 1b),
3. first GE EPI with AP PE direction (324 TRs; Figure 1a),
4. second AP GE scan (297 TRs),
5. B_0 field mapping scan (Figure 1d,e),
6. AP SE scan (3 TRs; Figure 1g),
7. PA SE scan (3 TRs; Figure 1h),
8. third AP GE scan (468 TRs).

Inhomogeneity in the B_0 field was minimized prior to 7 T fMRI data acquisition using the Siemens automated B_0 shimming procedure ($256 \times 256 \times 256$ mm field of view). Shim currents were calculated to minimize field variation within a $130 \times 170 \times 120$ mm³ region (i.e., the adjust volume) with an oblique-axial orientation centered on the brain (standardized by Auto-Align). To assess shim quality, the linewidth of water (full width at half-maximum [FWHM]) was measured in the Siemens Interactive Shim tab during each scanning session before fMRI data were acquired (for this study, mean linewidth across subjects = 60 Hz, $SD = 11$ Hz). Shim values were stored and applied across all scanning runs using a third-party stand-alone program (*shimcache*), to prevent any accidental loss of the B_0 shim between scans.

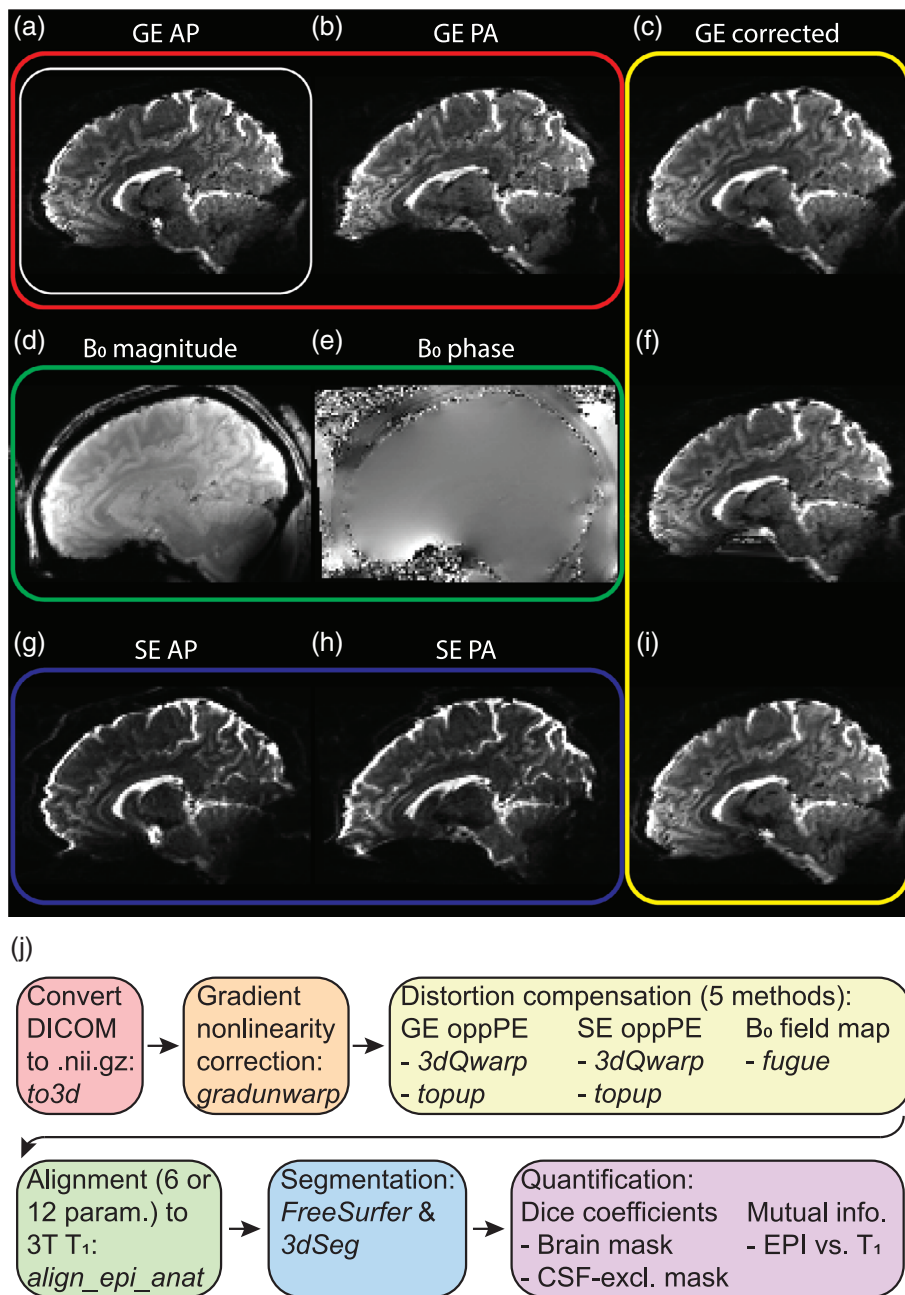
3 T structural MRI data were acquired on a Siemens MAGNETOM Prisma scanner (software version: VE11C). This scanner was equipped with two RF power amplifiers with a combined power of 40 kW, and body gradients with 80 mT/m maximum amplitude and 200 T/m/s maximum slew rate. Data were acquired using a Siemens 32 channel radio frequency head coil. T_1 - and T_2 -weighted anatomical scans (parameters listed in Table 1) were acquired in the first of two 3 T MRI scanning sessions.

TABLE 1 Scan parameters.

Scan	Field	TR (ms)	TE (ms)	Echo spacing (ms)	Flip angle (°)	Resolution	Partial Fourier	Slices	FOV (mm)
GE EPI	7 T	1,000	22.2	0.64	45	1.6 mm iso.	7/8	85	208 × 208
B_0 field map	7 T	642	4.08/5.1	—	32	1.6 mm iso.	6/8	85	208 × 208
SE EPI	7 T	3,000	60	0.64	90/180	1.6 mm iso.	7/8	85	208 × 208
T_1 anat.	3 T	2,500 ms	1.81/3.6/5.39/7.18	11.2	8	0.8 mm iso.	Off (phase) and 6/8 (slice)	208	256 × 256
T_2 anat.	3 T	3,200	564	3.86	Variable	0.8 mm iso.	Allowed (phase) and off (slice)	208	256 × 256

Abbreviations: anat., anatomical; EPI, echo planar imaging; GE, gradient echo; FOV, field of view; iso., isotropic; SE, spin echo; TE, echo time; TR, repetition time.

FIGURE 1 Data and processing pipeline. (a,b) Gradient echo (GE) data with opposite (anterior–posterior [AP] and posterior–anterior [PA], respectively) phase encoding directions. White box in (a) indicates that the GE AP data were the base dataset to which all distortion compensation methods were applied. All brain images are examples from the same parasagittal section in the same subject, after gradient nonlinearity correction was applied. (c) GE data corrected for geometric distortion using GE opposite phase encoding (oppPE) field map. (d,e) B_0 field map magnitude and phase data, respectively. (f) GE data with B_0 field map distortion compensation applied. (g,h) Spin echo (SE) oppPE data (AP and PA, respectively). (i) GE data after SE oppPE field map distortion compensation. (j) A summary of our data processing pipeline steps and software (italics). Arrows indicate the sequence in which processing steps were performed



2.3 | Data analysis and statistics

Our data processing pipeline is summarized in Figure 1j. All data processing steps were performed using either AFNI (Cox, 1996) (version 18.2.04) or FSL (Smith et al., 2004) (version 5.0.9), as noted below. Data were converted from DICOM to compressed (g-zipped) NIFTI format using AFNI's *to3d* program. We acquired at least three TRs for all EPI scans in order to allow the signal to reach steady state. To obtain a single time point for all EPI scans for the sake of computational efficiency, we took the temporal median of 3 TRs at the beginning or end of each scan (i.e., the time points closest to the respective field map scan[s], see below) using AFNI's *3dTstat*. Averaging was done to improve signal-to-noise; we used the median to prevent non-steady-state signals at the beginning of a scan from biasing the average.

In order to remove known geometric distortions due to gradient nonlinearities, we then performed gradient nonlinearity unwarping using *gradunwarp* (version 1.0.3; github.com/Washington-University/gradunwarp), with the warp field (also known as voxel displacement map) applied using AFNI's *3dNwarpApply*. This step is comparable to the correction for static gradient nonlinearities available within the HCP pipeline (Glasser et al., 2013). In Supplemental Figure 1, we show examples of voxel shift maps from gradient nonlinearity unwarping from a single subject. In Supplemental Table 1, we quantify the magnitude of gradient nonlinearity correction across all subjects. This shows that gradient nonlinearity distortion is often small for many voxels within the brain, but can be quite significant (up to about 4 mm) for some voxels. In our typical analysis path (i.e., in other studies), we

apply all geometric corrections within a single resampling step to minimize blurring. In the current study, we first applied gradient non-linearity correction and then separately applied B_0 inhomogeneity distortion compensation, which allowed us to specifically examine the performance of B_0 inhomogeneity distortion correction methods implemented in AFNI versus FSL.

2.3.1 | Distortion compensation

We then performed corrections for geometric distortion due to B_0 inhomogeneity on our 7 T GE EPI data using each of the following five methods:

1. GE oppPE field map correction (Andersson et al., 2003; Embleton et al., 2010; Morgan et al., 2004) via AFNI's *3dQwarp*.
2. GE oppPE correction with FSL's *topup*. Distortion correction in each of the two GE oppPE methods was applied to the median of TRs 1–3 from the first AP GE EPI scan (i.e., the scan closest in time to the GE oppPE field maps scans).
3. B_0 field map correction (Hunsche et al., 2004; Hutton et al., 2002; Jezzard & Balaban, 1995) in FSL's *fugue*, applied to the median of

TRs 295–297 from the second AP GE scan (the closest to the B_0 field map scan in time).

4. SE oppPE field map correction using AFNI's *3dQwarp*.
5. SE oppPE correction with FSL's *topup*. Distortion correction for both SE oppPE methods was applied to the median of TRs 1–3 from the third AP GE scan (the closest in time to the SE oppPE field maps scans).

Example brain images for GE oppPE correction using *3dQwarp* (Figure 2a) and *topup* (Figure 2b), B_0 field map correction using *fugue* (Figure 2c), and SE oppPE correction using *3dQwarp* (Figure 2d) and *topup* (Figure 2e) are provided, as well as uncorrected data (Figure 2f). We also present example images showing the difference between GE EPI data before and after distortion compensation in Supplemental Figure 2. The average voxel-wise difference between uncorrected and corrected data across subjects is shown for each method in Supplemental Figure 3.

The goal of our analysis was to facilitate comparisons of data quality between these five approaches for distortion compensation, which are current standards in the field. The details of each distortion compensation method are provided below (see Section 2.4 for a link to our published code for full details). Note that these methods are all

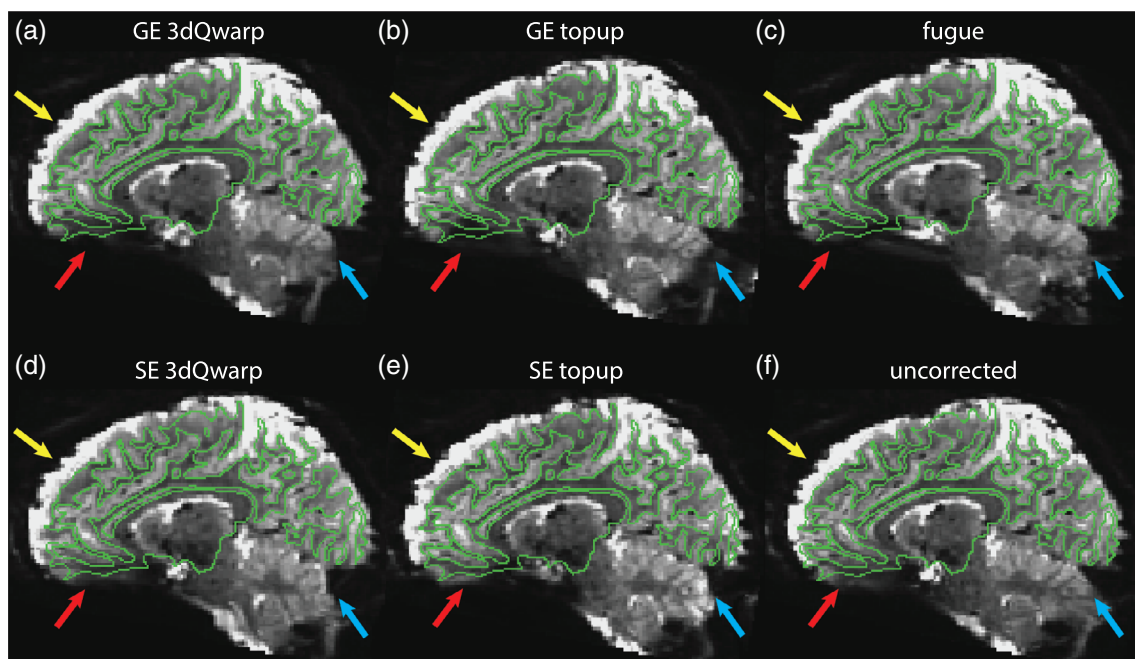


FIGURE 2 Distortion corrected echo planar imaging (EPI) data. Brain images are shown following distortion compensation using gradient echo (GE) opposite phase encoding (oppPE) data in AFNI's *3dQwarp* (a) or FSL's *topup* (b), B_0 field map data via FSL's *fugue* (c), and spin echo (SE) oppPE data in AFNI's *3dQwarp* (d) or FSL's *topup* (e), or without distortion correction (f). Green lines show the smoothed white matter surface model from FreeSurfer derived from the T_1 anatomical data, which illustrates good co-registration with the EPI data overall. Colored arrows indicate regions of interest with notable distortion (red: ventromedial prefrontal cortex [vmPFC], yellow: dorsomedial prefrontal cortex [dmPFC], blue: posterior regions), which are examined in subsequent analyses. All images show the same sagittal section from the same example subject, after gradient nonlinearity correction and alignment to the T_1 anatomical data. Note that the EPI data in this image exhibit greater blurring than those in Figure 1c,f,i (which reflect our true data quality), as the data here have undergone an additional resampling step to transform them into the space of the T_1 anatomy, to permit visualization of the smoothed white matter surface. Across panels, differences in distortion compensation and alignment are visible between methods

designed to correct geometric distortions in the PE direction only (on the order of several millimeters); distortions in the readout and through-slice directions (generally less than 0.1 mm) (Jezzard & Balaban, 1995) are not corrected by these methods and are not considered further in the present study.

For the GE and SE oppPE methods using AFNI's *3dQwarp*, both the AP and PA scans were independently masked using AFNI's *3dAutomask* to remove nonbrain image regions. Next, the warp field for distortion compensation was calculated using *3dQwarp* with the *-plusminus* flag (indicating that the desired undistorted brain image is "in between" the AP and PA scans). This program iteratively calculates the difference in distortion between AP and PA data by fitting cubic polynomials within corresponding three dimensional rectangular image regions of progressively smaller size, starting with the entire volume, down to a minimum region size in our study of 9 mm. Progressive blurring was applied to the patches in each iteration using a spatial median filter. *3dQwarp* allows for progressive blurring to avoid matching fine spatial details in early iterations when attempting to calculate distortion across large image regions. On the first iteration (whole volume), data were median filtered within a radius of 1.6 mm. In subsequent iterations, the median filter radius was set to be 5% of the patch size, such that less blur was applied to smaller image regions. Distortion compensation of the GE EPI scan was then performed by applying the resulting warp field using AFNI's *3dNwarpApply* with sinc interpolation for the final resampling step. For full details on *3dQwarp*, see afni.nimh.nih.gov/pub/dist/doc/program_help/3dQwarp.html.

For distortion based on GE and SE oppPE field maps using FSL's *topup* (Andersson et al., 2003), the warp field was calculated using the default *topup* parameters (i.e., those provided by FSL within the *b02b0.cnf* file). The *topup* method involves calculating the difference in geometric distortion between AP and PA scans across multiple iterations, with progressively finer resolution fits using B-splines. The resolution (knot spacing) for the splines varied across iterations from 19.2 to 3.2 mm in our study. Data were progressively blurred across iterations using a Gaussian kernel with an FWHM ranging from 8 to 0 mm (i.e., no smoothing) for lower to higher resolution fits. Similar to *3dQwarp*, progressive blurring helps to prevent *topup* from matching fine details in early iterations when calculating distortion across larger image regions. Here, data in the first five iterations (i.e., fit with lower resolution) were sub-sampled by a factor of two, to speed up computation time. Prior to *topup*, both the AP and PA scans were zero padded with one additional slice in the superior direction, to obtain an even number of slices (as required for the voxel subsampling). Geometric distortion within the GE EPI scan was corrected based on the calculated warp field using FSL's *applytopup*, with the Jacobian modulation method for intensity restoration and cubic B-spline interpolation. The added empty slice was removed after distortion compensation. This step is analogous to the oppPE method for geometric distortion compensation of fMRI data implemented in the HCP minimal preprocessing pipeline (Glasser et al., 2013). For more details on *topup*, see fsl.fmrib.ox.ac.uk/fsl/fslwiki/topup/TopupUsersGuide.

For the B_0 field map method using FSL's *fugue*, nonbrain regions of the magnitude portion of the B_0 field map were removed using FSL's *bet*. The difference between the phase portions of the B_0 field map scans with different TEs were exported by the scanner automatically. This phase difference map was then masked within the extracted brain region, converted from scanner units to radians per second using FSL's *fsl_prepare_fieldmap* tool (which also includes phase unwrapping), and then blurred (i.e., median filtered, radius = 1.6 mm) using AFNI's *3dMedianFilter*. This blurring step was done in order to reduce noise in the field map, especially in regions near the outer edge of the brain. Distortion compensation of the GE EPI data was then performed using this phase map via FSL's *fugue*. For comparison with oppPE methods, we converted phase difference maps to voxel shift maps by multiplying by total readout time and dividing by 2π . We note that unlike *3dQwarp* and *topup*, the *fugue* method produces a voxel shift map in which the values are zero outside of the brain (Figure 5). For full details on *fugue*, please see fsl.fmrib.ox.ac.uk/fsl/fslwiki/FUGUE/Guide.

Our primary analysis (reported in the Analysis #1: main study section of the Results) assumes there was no head motion between each field map and the corresponding GE EPI scan, and that any difference between oppPE scan pairs is caused by geometric distortion and not head motion (Hutton et al., 2002). Thus, no alignment between field map and GE EPI scans was performed prior to distortion compensation, in order to avoid any spurious 'correction' of differences between scans that was in fact caused by geometric distortion (rather than head motion). We performed an additional analysis that included an initial alignment between EPI and field map data, described below as Analysis #2, in order to examine the impact of this methodological decision.

2.3.2 | Alignment

Following distortion compensation, we aligned GE EPI data and T_1 anatomical scans using AFNI's *align_epi_anat.py* function (Figures 2 and 3c). This alignment method uses a local Pearson correlation (lpc) cost function (Saad et al., 2009), which seeks to co-register brain structures based on correlations between voxels within a small neighborhood (several millimeters). This alignment procedure is similar to boundary-based registration (Greve & Fischl, 2009), such as is implemented in the HCP minimal preprocessing pipeline (Glasser et al., 2013). We performed rigid body alignment (six-parameter: x, y, z, roll, pitch, yaw) to the T_1 for EPI data from each of the five distortion compensation methods above. We used a rigid body alignment procedure in order to preserve the geometric properties of the GE EPI datasets, to facilitate clear comparison between the various distortion compensation methods. While others, including the original Young Adult HCP (Vu et al., 2015), have used 9- or 12-parameter alignment methods to co-register 7 T fMRI and 3 T anatomical data, in the current study, we chose to use a six-parameter alignment method along with a separate gradient nonlinearity correction step. In this way, we omitted arbitrary scaling of our 7 T EPI data to match the 3 T

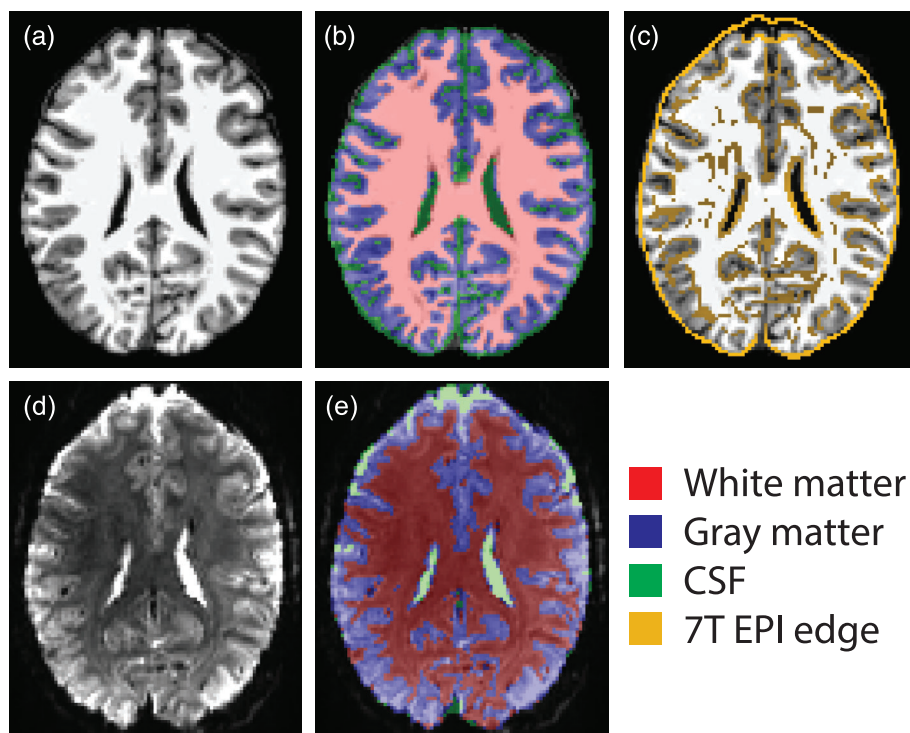


FIGURE 3 Alignment and segmentation of T_1 (a–c) and echo planar imaging (EPI) data (c–e). Transparent colored overlays in (b,e) show binary masks for gray matter (blue), white matter (red), and cerebrospinal fluid (CSF; green) as a result of tissue segmentation. Yellow lines in (c) show edges from 7 T gradient echo (GE) EPI (using AFNI's *3dedge3*) overlaid on T_1 data, to show alignment. All brain images are examples from the same axial section in the same subject, after gradient nonlinearity correction, geometric distortion compensation, and co-registration

anatomy, and instead focused on quantifying the correction of geometric distortions based on first principles.

In addition to the five distortion-compensation conditions, we included two further alignment-only analysis conditions in which the GE EPI data were aligned with the anatomical scans without any initial distortion compensation. In the six-parameter alignment-only condition, EPI data without distortion compensation were aligned with the T_1 anatomy using six-parameter (rigid-body) registration with the *lpc* cost function, as above. In contrast, the 12-parameter alignment only condition used 12 parameter affine alignment (six additional parameters for scaling and shearing). We were motivated to include the 12-parameter alignment method to determine the extent to which the addition of the six scaling and shearing parameters would mirror geometric distortion compensation performed with oppPE or B_0 field mapping methods.

This procedure yielded a total of seven GE EPI datasets per subject for our analyses (five distortion compensated versions detailed above, plus 6- and 12-parameter alignment-only versions). We refer to these as the seven different analysis conditions below, as they form the basis of our comparison of different approaches for geometric distortion compensation.

Prior to alignment, the T_1 and T_2 anatomical data were processed using the HCP minimal preprocessing pipeline (Glasser et al., 2013) (version 3.22.0), including gradient nonlinearity correction with *gradunwarp* and skull stripping. Note that no correction for geometric distortion due to B_0 inhomogeneity was performed for these anatomical data, as any such distortions are expected to be minimal (<0.1 mm) (Studholme et al., 2000). Although T_2 -weighted scans have a more similar intensity profile to the GE EPI data, T_1 anatomical scans are currently more widely used in the field of human functional

neuroimaging, and robust approaches for aligning EPI and T_1 data have been developed (Saad et al., 2009). Thus, we chose to use the T_1 -weighted scan as our anatomical reference in our primary analysis in order to increase the generalizability of our results. We also conducted an additional analysis (Analysis #4 below) using the T_2 -weighted scan as our anatomical reference, for comparison purposes. We corrected intensity inhomogeneities across the brain in the T_1 anatomical data using AFNI's *3dUnifize*.

2.3.3 | Tissue segmentation

In order to facilitate a more detailed analysis of how different distortion compensation methods performed in gray matter and white matter regions, we next segmented different tissue types within our T_1 and EPI data, with the goal of obtaining brain tissue masks with CSF regions excluded. We performed tissue segmentation for each subject using the T_1 and T_2 anatomical scans to define individual white matter and pial surfaces in FreeSurfer (Dale, Fischl, & Sereno, 1999; Dale & Sereno, 1993) (version 5.3.0) as part of the HCP minimal preprocessing pipeline (Glasser et al., 2013) (Figure 3a,b). For each of the seven analysis conditions in each subject, we then transformed both the T_1 and FreeSurfer's segmentation data (*wmparc*) into the space of the GE EPI scan using the alignment information (obtained above) via AFNI's *3dAllineate*. Individual binary masks for gray matter and white matter were defined from the transformed *wmparc* file based on FreeSurfer's anatomical labels (surfer.nmr.mgh.harvard.edu/fswiki/FsTutorial/AnatomicalROI/FreeSurferColorLUT). To define binary masks for cerebrospinal fluid (CSF), we summed the gray and white matter masks, blurred the summed data using AFNI's *3dmerge*

(FWHM = 0.5 mm), and then masked the blurred data at a value of 0.2 to create a binary mask that included the region surrounding the brain (putative CSF). We then summed this mask with a binary mask of the ventricles from FreeSurfer's *wmparc* file, and subtracted the gray and white matter masks to obtain a CSF mask. Gray matter, white matter, and CSF masks from the T_1 anatomy were used to aid segmentation of the 7 T GE EPI data (below).

To segment the 7 T GE EPI data into gray matter, white matter, and CSF regions (Figure 3d,e), we first corrected spatial inhomogeneities in the GE EPI data using AFNI's *3dUnifize*, and then derived a whole-brain mask using AFNI's *3dAutomask*. We then segmented the 7 T fMRI data from each analysis condition in each subject into gray matter, white matter, and CSF using AFNI's *3dSeg* function, with the gray matter, white matter, and CSF masks from the T_1 scan (above) as seed data (*cset* file). Tissue masks from the 7 T fMRI data were median filtered with a radius of 1.6 mm using AFNI's *3dMedianFilter* to reduce noise.

2.3.4 | Dice coefficients

To quantify alignment between T_1 anatomical and GE EPI data (and thus the effectiveness of distortion compensation), we calculated the overlap between each subject's T_1 and fMRI data in each of the seven analysis conditions using Dice coefficients via AFNI's *3ddot* function. The Dice coefficient is a measure of how well two binary datasets overlap in three-dimensional space. This metric varies between zero (no overlap) and one (identity) and is calculated by taking the intersection of the two datasets, multiplying by two, and then dividing by the total number of voxels in both scans. Dice coefficients were calculated using two different types of binary masks of the 3 and 7 T data: (a) a whole-brain mask (including some CSF) using AFNI's *3dAutoMask*, and (b) a CSF-excluded mask based on the segmented T_1 and fMRI data (i.e., including white matter [red] and gray matter [blue], but not CSF [green] regions, as shown in Figure 3b,e). Note that the EPI masks were generated from the distortion corrected EPI data themselves, and not from the corresponding field map scans. We also note that both residual distortion and signal loss due to through-slice dephasing will result in lower Dice coefficient values, indicating poorer agreement with the corresponding T_1 scan.

2.3.5 | Mutual information

We also quantified alignment quality by calculating mutual information between the T_1 and fMRI data for each of the seven analysis conditions in each subject. This metric, which comes from the information theory literature, reflects the similarity of two datasets by quantifying how much is learned about the second dataset from knowing a value in the first. Mutual information is often used to assess multimodal brain image registration (Studholme, Hill, & Hawkes, 1999), and should be maximal for two identical datasets that are perfectly aligned. Specifically, mutual information is defined as the difference

between the joint entropy and the sum of the marginal entropies for two datasets. Compared to Dice coefficients, mutual information is more sensitive to differences in alignment in internal brain structures. Prior to calculating mutual information, we excluded nonbrain regions of the T_1 and EPI data using the whole-brain masks described above (intensity values for regions outside the mask were set to zero). We computed mutual information using the *mutInfo* function in MATLAB (mathworks.com/matlabcentral/fileexchange/35625-information-theory-toolbox).

2.3.6 | Region of interest analyses

To examine the effect of different distortion compensation methods within specific regions of interest (ROIs), we created spherical binary masks in ventromedial prefrontal cortex (vmPFC; radius = 26 mm; Figure 6d), dorsomedial prefrontal cortex (dmPFC; radius = 21 mm; Figure 7d), and a large posterior region encompassing the occipital pole and posterior cerebellum (referred to as the posterior ROI; radius = 34 mm; Supplemental Figure 10). In each subject, we took the intersection of each of these ROIs with the whole-brain masks from the T_1 and EPI scans for each of the seven analysis conditions to create whole-ROI masks; in Supplemental Figure 4, we show examples of whole-ROI masks from both vmPFC (a and b) and dmPFC (e and f). We also took the intersection between each of the spherical ROIs and the CSF-excluded masks for the T_1 and EPI data in each condition to define CSF-excluded ROI masks (Supplemental Figure 4c,d,g,h). We then computed the Dice coefficient between these T_1 and EPI ROI masks, as described for the whole brain above. Finally, we took the intersection between each spherical ROI mask and the T_1 anatomical and EPI scan data themselves, and then computed mutual information between the T_1 and EPI data within each ROI for each analysis condition in each subject, excluding nonbrain regions as in our whole-brain mutual information calculation above.

2.3.7 | Additional analyses

In addition to our main study (Analysis #1), we conducted six further analyses focused on the following: (a) prealigned data, (b) single-band reference data, (c) using a T_2 reference anatomy, (d) PA PE data, (e) Young Adult HCP data, and (f) correcting SE data. Methodological details for these analyses are presented in the Supplemental methods.

2.3.8 | Statistics

Statistical analyses were performed in MATLAB (version 2017b). Analyses of variance (ANOVAs) were performed using the *anovan* function, with subjects treated as a random effect, and the seven analysis conditions (i.e., the five different distortion compensation methods,

plus the 6- and 12-parameter alignment-only data) as a within-subjects factor. Normality and homogeneity of variance were assessed by visual inspection of the data (e.g., Supplemental Figure 6). Post hoc comparisons between analysis methods were performed using paired two-tailed *t* tests, with false discovery rate (FDR) correction for 21 multiple comparisons (pair-wise comparisons between the seven analysis conditions).

Because the effects of interest (i.e., differences between distortion compensation methods) were within- rather than between-subjects, we used within-subjects error bars (Morey, 2008) to visualize the variance in each analysis condition, thereby excluding the between-subjects variance for display purposes. To do so, we used an established method (Morey, 2008) that involved subtracting the mean value for each subject (across all analysis conditions) from all data points for that individual, and then adding the grand mean (across all subjects and conditions).

Across all analyses, data were visualized in AFNI using default settings for display purposes (i.e., image histograms are scaled so that black $\leq 2\%$, white $\geq 98\%$), unless otherwise noted. Brain images are shown in neurological convention (i.e., left is left).

2.4 | Code and data availability

We have made our analysis code publicly available on GitHub (github.com/mpschallmo/DistortionCompensation). Our imaging data are available from the HCP Connectome Coordination Facility (intradb.humanconnectome.org; first Psychosis HCP data release planned for third quarter, 2021).

3 | RESULTS

3.1 | Analysis #1: Main study

3.1.1 | Whole-brain analysis

To compare different distortion compensation methods, we first examined the overlap between whole-brain masks obtained from 7 T GE EPI data that had been corrected for geometric distortion and T_1 -weighted anatomical data (T_1 hereafter), following co-registration (Figure 2; Figure 3c). Data from seven different conditions (i.e., paths

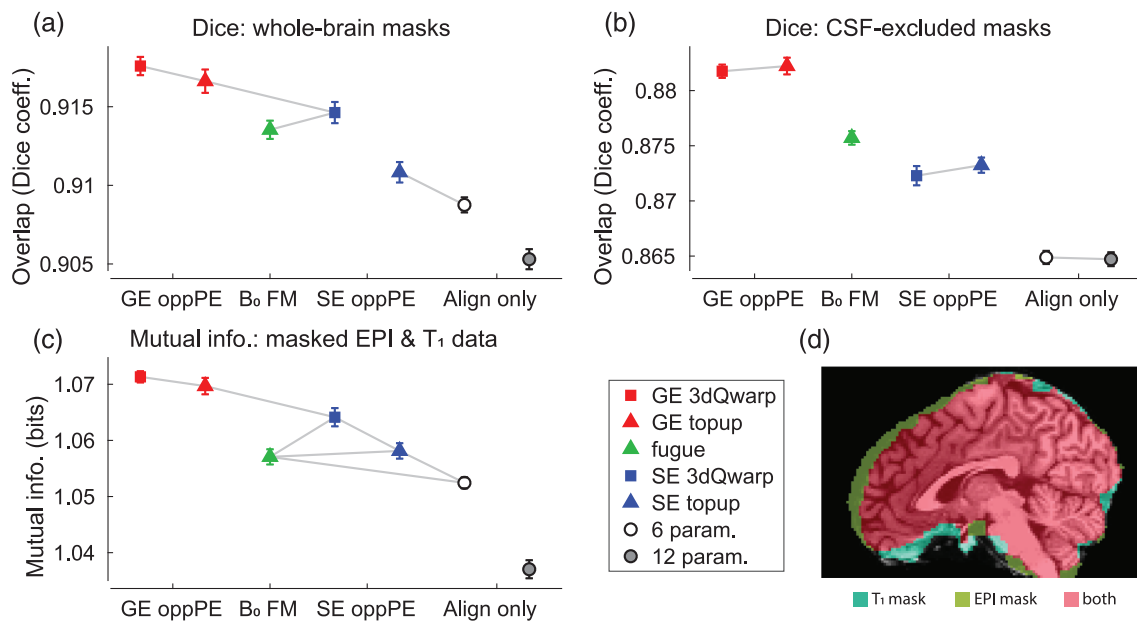


FIGURE 4 Main whole-brain results. (a) Overlap (Dice coefficient) between gradient echo (GE) echo planar imaging (EPI) and T_1 whole-brain masks, across different distortion compensation methods. Gray lines indicate conditions that do not differ significantly (post hoc paired *t* tests, threshold $p < .05$, false discovery rate [FDR] corrected). X-axis labels: GE oppPE = GE opposite phase encoding field map (red), B₀ FM = B₀ field map (green), SE oppPE = spin echo opposite phase encoding field map (blue), Align only = alignment-only (no explicit geometric distortion compensation). (b) Same, but for binary whole-brain masks with regions of cerebrospinal fluid (CSF) excluded, following tissue segmentation. (c) Mutual information between GE EPI and T_1 scan data, within the respective whole-brain masks. Squares show data corrected using AFNI, triangles show data from FSL, and circles show alignment-only data. Error bars are SEM calculated within subjects (Morey, 2008). (d) Example T_1 anatomical image with overlaid whole-brain masks: T_1 (teal), EPI (yellow), and T_1 -EPI overlap (red). The Dice coefficient analysis in (a) quantified the agreement between EPI and T_1 masks (i.e., red vs. teal and yellow), whereas (b) did the same after excluding CSF regions. EPI and T_1 masks do not overlap perfectly; midline CSF may be included in the automated EPI whole-brain mask (yellow, dorsal), which prompted us to examine CSF-excluded masks (b). Further, through-slice dephasing leads to EPI signal loss in orbital frontal cortex (cyan, ventral), which prompted examination of the ventromedial prefrontal cortex (vmPFC) region of interest (ROI) in Figure 6. All of the tested distortion compensation methods improved agreement between functional MRI (fMRI) and T_1 datasets. For our particular dataset, GE oppPE field maps (red) tended to produce the best results

to EPI- T_1 registration) were examined (Figure 1j), including those obtained using five different distortion correction methods, and two alignment-only datasets (6- and 12-parameter alignment). Example brain images corrected using GE oppPE (*3dQwarp* and *topup*), B_0 field map (*fugue*), and SE oppPE methods (*3dQwarp* and *topup*), as well as uncorrected data, are shown in Figure 2. Binary masks were generated from both the EPI data and the co-registered T_1 anatomy in each of the seven analyses separately, in each of our 31 subjects. Overlap between EPI and T_1 masks (Figure 4d) was quantified using the Dice coefficient; higher Dice coefficients reflect more-effective distortion compensation.

Dice coefficients for the whole-brain masks were significantly different across analysis conditions ($F_{6,30} = 42.7$, $p = 4 \times 10^{-32}$), as shown in Figure 4a (see also Supplemental Figure 6 for a visualization of all data points). This indicates that the method of distortion compensation significantly affected the degree to which whole-brain masks from EPI and T_1 anatomical scans overlapped. Post hoc paired t tests (FDR corrected for 21 comparisons between conditions) revealed that the overlap between EPI and T_1 anatomical masks was highest and comparable for the two GE oppPE methods using AFNI's *3dQwarp* and FSL's *topup* (red symbols). Dice coefficients were lower when using the B_0 field map (using FSL's *fugue*; green triangle) and SE oppPE (via *3dQwarp*; blue square). Note that in Figure 4, gray lines indicate conditions that do not differ significantly based on post hoc tests (i.e., conditions that do differ significantly are not linked by gray lines; all significant paired t_{30} values ≥ 2.82 , FDR-corrected p -values $\leq .042$). Lower Dice coefficients were observed for the SE oppPE data corrected using *topup* (blue triangle), which did not differ from the uncorrected data using only a six-parameter alignment (white circle). Dice coefficients for whole-brain masks were lowest for the data using a 12-parameter alignment only (gray circle).

Next, we examined overlap of tissue masks with CSF regions excluded (see Section 2), in order to more closely examine how different distortion compensation methods performed in regions of gray matter and white matter. Dice coefficients for CSF-excluded masks differed significantly between different analysis conditions ($F_{6,30} = 91.5$, $p = 5 \times 10^{-52}$; Figure 4b), showing that the agreement between non-CSF brain regions from the EPI and T_1 anatomical scans depended on the method of distortion compensation that was used. Post hoc paired t tests revealed that the overlap for non-CSF regions was highest when using GE oppPE field maps for distortion compensation (via either AFNI's *3dQwarp* or FSL's *topup*; red symbols; all significant paired t_{30} values ≥ 2.84 , FDR-corrected p -values $\leq .032$). The overlap for the CSF-excluded masks was lower when distortion compensation was performed using a B_0 field map (via FSL's *fugue*; green triangle) or SE oppPE field map (in either AFNI's *3dQwarp* or FSL's *topup*; blue symbols), and lowest for the alignment-only data (using either six-parameter [white circle] or 12-parameter alignment methods [gray circle]).

We further compared distortion compensation methods by calculating the mutual information between fMRI and T_1 data across the whole brain, as higher mutual information reflects better alignment. Compared to the Dice coefficient, mutual information is more

sensitive to differences in the alignment of internal brain structures, as it is based on the intensity of all voxels within the brain. Within the whole-brain masks, mutual information between EPI and T_1 anatomical scans was significantly different across analysis conditions ($F_{6,30} = 35.1$, $p = 7 \times 10^{-28}$; Figure 4c), reflecting a difference in alignment quality for different distortion compensation methods. In particular, post hoc tests revealed that mutual information across the brain was generally highest when using the GE oppPE field map methods for distortion compensation (red squares; all significant paired t_{30} values ≥ 3.48 , FDR-corrected p -values $\leq .017$). Mutual information was generally comparable between B_0 field map, SE oppPE methods and the six-parameter alignment-only data (white circle). The 12-parameter alignment-only method (gray circle) yielded lower mutual information compared to all other conditions.

3.1.2 | ROI analyses

Thus far, our analyses have focused on metrics to quantify distortion compensation across the whole brain. However, there is significant variability in the amount of geometric distortion due to B_0 inhomogeneity (and in the voxel shift applied by different correction methods) between brain regions, as shown in Figure 5 and Supplemental Figure 7. Such regional variability is quantified in Supplemental Figure 8, which shows example histograms of voxel shift data obtained using different distortion compensation methods across brain regions from a single subject. Further, Supplemental Figure 9 summarizes the voxel shift data (mean, median, SD , and maximum absolute shift) from different distortion compensation conditions and different brain regions across all subjects.

To examine whether our results might be affected by regional variability in distortion due to B_0 inhomogeneity across the brain, we next compared the performance of different distortion compensation methods within specific ROIs; specifically, the vmPFC (Figure 6d, Supplemental Figure 4a,b), the dmPFC (Figure 7d, Supplemental Figure 4c,d), and a posterior ROI which included the occipital pole and posterior cerebellum (Supplemental Figures 7 and 10). Each of these ROIs exhibit substantial geometric distortion for EPI scans with an AP PE direction, but in vmPFC there is also significant signal dropout due to through-slice dephasing (Figures 2 and 5a). Thus, we examined the same distortion compensation metrics used above (Dice coefficients and mutual information) but restricted to these ROIs, to assess how different distortion compensation methods may perform in regions with significant distortion, both with and without additional dropout.

We first asked how different distortion compensation methods would perform in vmPFC (Figure 6d, Supplemental Figure 4a,b), a region that shows substantial geometric distortion and dropout. In particular, we were interested in whether SE oppPE field maps might outperform GE oppPE methods, as superior distortion correction for SE field maps has been theorized on the basis that the 180° refocusing pulse reduces dropout in SE sequences (Holland et al., 2010). Dice coefficients for vmPFC masks (Figure 6a,b) showed higher overlap between T_1 anatomical and EPI data for SE oppPE field

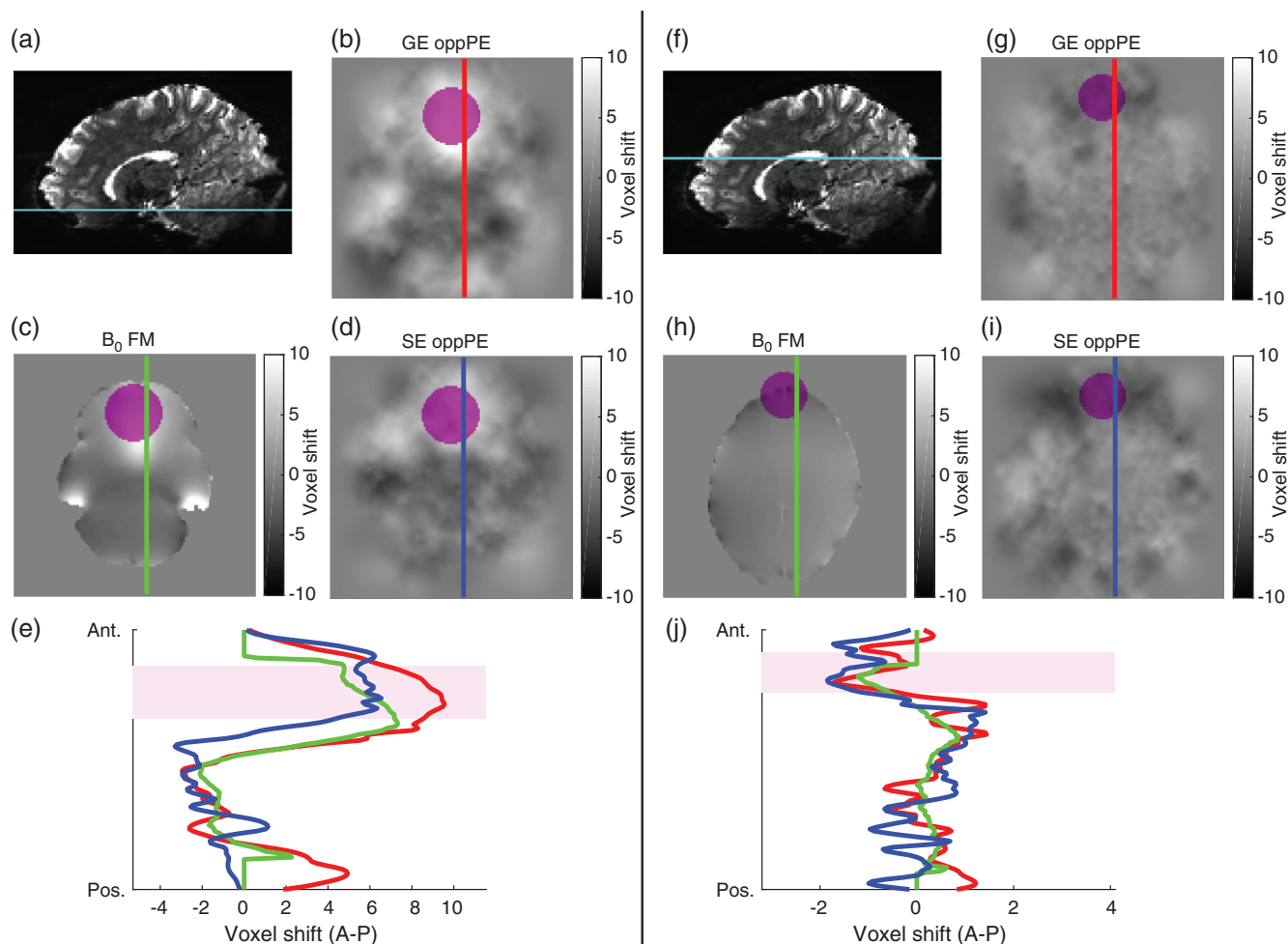


FIGURE 5 Voxel shift maps for ventral and dorsal regions. (a–e) Ventral regions. Example voxel shift maps from the same ventral axial section (cyan line; (a)) in the same subject are shown for distortion compensation based on gradient echo (GE) oppPE (b), B_0 field map (c), and spin echo (SE) oppPE (d) correction methods. Color bar indicates voxel shift in the anterior–posterior (positive–negative) direction. Colored vertical lines indicate the positions of the voxel shift data plotted in (e). Magenta regions in (b–e) show the ventromedial prefrontal cortex region of interest (ROI) used below (Figure 6). (f–j) Same as in (a–e), but for a more dorsal section. Magenta regions in (g–j) show the dorsomedial prefrontal cortex ROI used below (Figure 7). GE and SE oppPE corrections in these examples were performed with AFNI's *3dQwarp*. Note that the x-axes differ in (e) and (j). Differences in voxel shifts between correction methods are apparent, particularly in regions such as ventromedial and dorsomedial prefrontal cortex

map methods (blue) versus GE oppPE (red), with B_0 field map correction using *fugue* (green) in the middle (ANOVAs, main effects of condition for whole-vmPFC masks and CSF-excluded masks, $F_{6,30} > 46.7$, p -values $< 3 \times 10^{-34}$). However, there was little or no advantage for any of these methods when compared to scans with no distortion compensation applied at all (6- or 12- parameter alignment only; white and gray, respectively). This suggests that although SE oppPE methods yielded the best agreement between T_1 and EPI data in the vmPFC region, distortion compensation may not substantially improve T_1 -EPI agreement in vmPFC, compared to no correction. Further, mutual information between T_1 and EPI data in vmPFC was not significantly different across conditions (ANOVA, main effect, $F_{6,30} = 0.99$, $p = .4$), suggesting that none of the distortion compensation methods we tested had a substantial effect on T_1 -EPI agreement in vmPFC according to this metric.

Next, we compared the performance of different distortion compensation methods within a region that also shows substantial geometric distortion due to B_0 inhomogeneities, but less dropout due to through-slice dephasing, dmPFC (Figure 7d, Supplemental Figure 4c,d). Here, we found results that were more similar to our whole-brain results, as compared to those from vmPFC. In particular, we saw substantial differences in dmPFC across distortion compensation methods for all three of our metrics (ANOVAs, main effects of condition for whole-dmPFC masks, CSF-excluded masks, and mutual information, $F_{6,30} > 14.1$, p -values $< 4 \times 10^{-13}$; Figure 7), with GE oppPE methods (red) generally yielding the best agreement between T_1 and EPI data in dmPFC. Thus, we conclude that in regions such as dmPFC in which there is significant geometric distortion (but not dropout), GE oppPE methods may show slight advantages over other distortion compensation techniques,

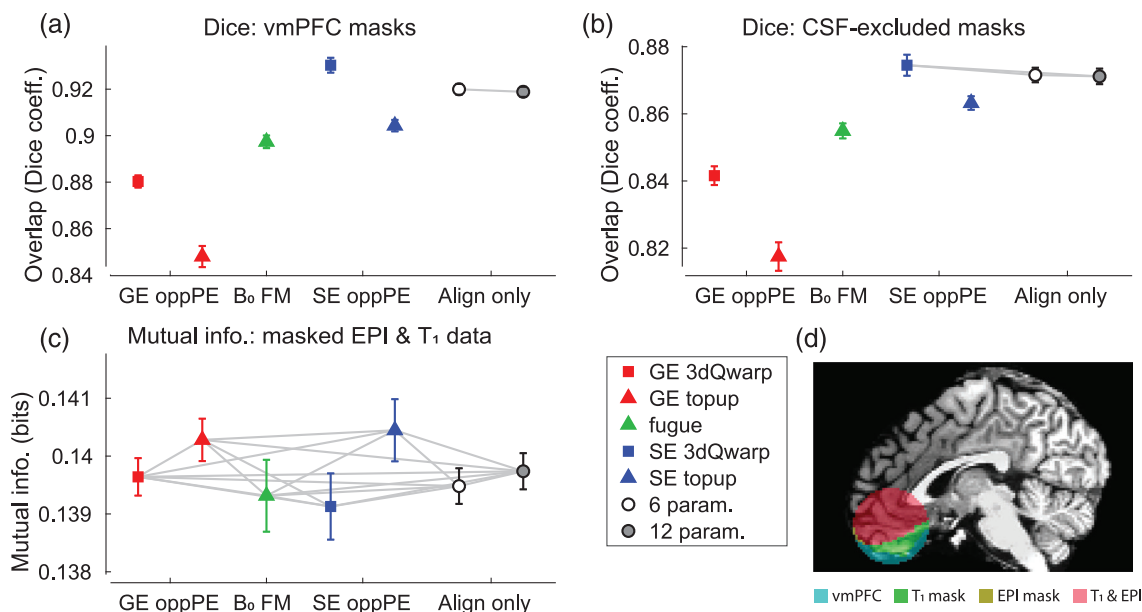


FIGURE 6 Results in ventromedial prefrontal cortex (vmPFC). (a) Overlap (Dice coefficient) between gradient echo (GE) echo planar imaging (EPI) and T₁ binary masks restricted to vmPFC, across different distortion compensation methods. Gray lines indicate conditions that do not differ significantly (post hoc paired *t* tests, threshold $p < .05$, false discovery rate [FDR] corrected). X-axis labels: GE oppPE = gradient echo opposite phase encoding field map (red); B₀ FM = B₀ field map (green); SE oppPE = spin echo opposite phase encoding field map (blue); Align only = alignment-only (no explicit geometric distortion compensation). (b) Same, but for binary masks in vmPFC with regions of cerebrospinal fluid (CSF) excluded, following tissue segmentation. (c) Mutual information between GE EPI and T₁ scan data in the vmPFC ROI. Squares show data corrected using AFNI, triangles show data from FSL, circles show alignment-only data. Error bars are SEM calculated within subjects (Morey, 2008). (d) Example T₁ anatomical image with overlaid vmPFC masks: whole-region of interest (ROI) (teal), T₁ (green), EPI (yellow), and T₁-EPI overlap (red). The Dice coefficient analysis in (a) quantified the agreement between EPI and T₁ masks (i.e., red vs. green and yellow), whereas (b) did the same after excluding CSF regions. SE oppPE methods yielded somewhat better T₁-EPI agreement than GE or B₀ methods for whole-vmPFC masks (a) and CSF-excluded masks in vmPFC (b), but little or no advantage over alignment-only methods (gray and white), and there were no significant differences in mutual information across methods (c). This suggests a modest advantage for SE oppPE correction over other methods within regions with substantial dropout, but even SE oppPE correction may not yield substantially better T₁-EPI agreement as compared to uncorrected EPI data (i.e., alignment only)

similar to the pattern of results from our earlier whole-brain analysis.

Finally, we examined how distortion compensation varied in posterior brain regions across our seven analysis conditions (Supplemental Figures 7 and 10). Like dmPFC, posterior regions exhibit geometric distortion due to B₀ inhomogeneity, but less through-slice dephasing than in vmPFC. Results within the posterior ROI differed significantly across condition (ANOVAs, main effects of condition for whole-ROI masks, CSF-excluded masks, and mutual information, $F_{6,30} > 10.1$, p -values $< 1 \times 10^{-9}$), and were generally similar to those in dmPFC. Agreement between T₁ and EPI data in posterior regions tended to be higher in the five GE oppPE, B₀ field map, and SE oppPE conditions, as compared to the alignment-only conditions, but results were similar between the five distortion compensation conditions overall.

3.2 | Analysis #2: Prealigned data

Because our scans were acquired in a fixed order, we considered whether differences in head motion might have biased our results in

favor of the GE oppPE data, which was acquired near the beginning of the session (approximately 1.25 hr in total length), rather than the B₀ field map or SE oppPE data, which were acquired near the end. Specifically, if subjects tended to move more during the B₀ field map and SE oppPE scans, or moved more between these scans and the GE EPI scans on which distortion compensation was performed, then this might degrade the quality of distortion compensation for the B₀ field map and SE oppPE methods as compared to the GE oppPE method.

To explore this issue, we performed our analyses again after first aligning all field map and 7 T GE fMRI scans to the magnitude portion of the B₀ field map. We applied all five distortion compensation methods to the same 7 T GE EPI scan, to mitigate any possible bias caused by the fixed scanning order. Whether or not the GE EPI and field map data were initially aligned had very little impact on our whole brain results (Supplemental Figure 11). After initial alignment, all distortion compensation methods improved agreement between fMRI and T₁ data (ANOVAs, main effects of condition, $F_{6,30} > 35.7$, p -values $< 3 \times 10^{-28}$) as compared to the alignment-only conditions, with the GE oppPE field maps showing the strongest performance, similar to the results in our main analysis (Figure 4).

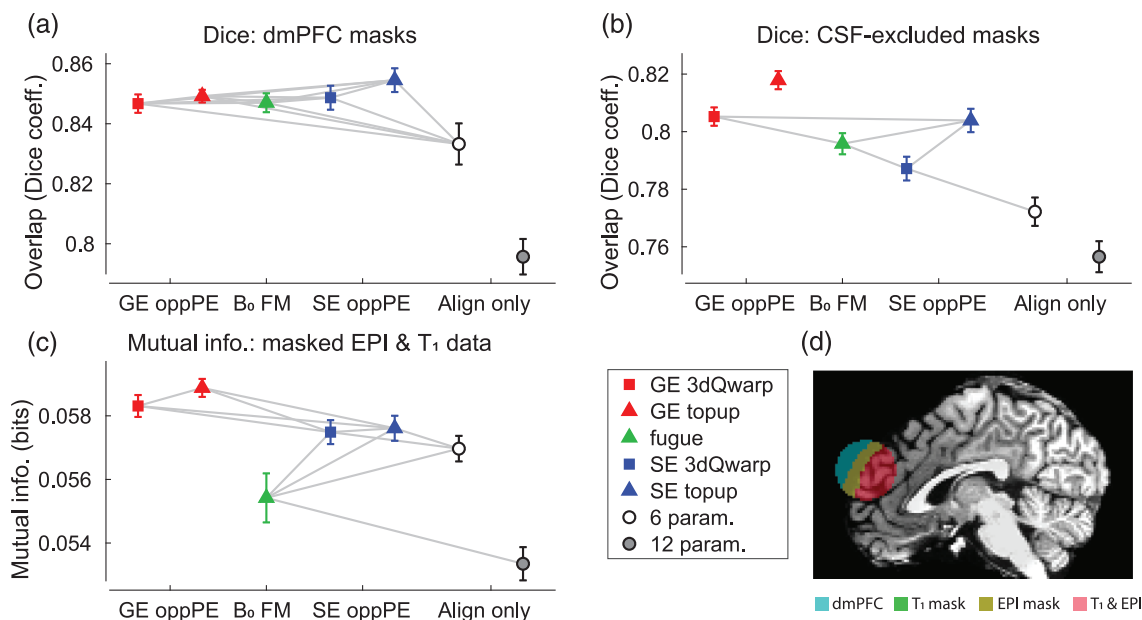


FIGURE 7 Results in dorsomedial prefrontal cortex (dmPFC). (a) Overlap (Dice coefficient) between gradient echo (GE) echo planar imaging (EPI) and T₁ binary masks restricted to dmPFC, across different distortion compensation methods. Gray lines indicate conditions that do *not* differ significantly (post hoc paired *t* tests, threshold $p < .05$, false discovery rate (FDR) corrected). X-axis labels: GE oppPE = gradient echo opposite phase encoding field map (red), B₀ FM = B₀ field map (green), SE oppPE = spin echo opposite phase encoding field map (blue), Align only = alignment-only (no explicit geometric distortion compensation). (b) Same, but for binary masks in dmPFC with regions of cerebrospinal fluid (CSF) excluded, following tissue segmentation. (c) Mutual information between GE EPI and T₁ scan data in the dmPFC Region of interest (ROI). Squares show data corrected using AFNI, triangles show data from FSL, circles show alignment-only data. Error bars are SEM calculated within subjects (Morey, 2008). (d) Example T₁ anatomical image with overlaid dmPFC masks: whole-ROI (teal), T₁ (green), EPI (yellow), and T₁-EPI overlap (red). The Dice coefficient analysis in (a) quantified the agreement between EPI and T₁ masks (i.e., red vs. green and yellow), whereas (b) did the same after excluding CSF regions. T₁-EPI agreement was generally highest in dmPFC for EPI data corrected using GE oppPE field maps (red) similar to our whole-brain results (Figure 4)

3.3 | Analysis #3: Single-band reference

Alignment and segmentation of GE EPI data may depend on image contrast (e.g., gray matter vs. white matter intensity). To explore the role of image contrast in our results, we repeated our main whole-brain analyses using the single-band reference data in place of the multiband 7 T GE EPI data for alignment, segmentation, and quantification purposes, as image contrast was higher in the single-band reference (Supplemental Figure 5). The patterns of results for the single-band reference data (ANOVAs, main effects of condition, $F_{6,30} > 35.2$, p -values $< 5 \times 10^{-28}$; Supplemental Figure 12) were very similar to those obtained with multiband GE EPI in the main analysis (Figure 4), suggesting that the quality of the alignment and segmentation of our 7 T data were not limited by image contrast in the multiband scans.

3.4 | Analysis #4: T₂ Reference anatomy

The alignment between GE EPI data and an anatomical reference, and therefore our subsequent quantification of distortion compensation metrics (Dice coefficients and mutual information), may depend on the chosen anatomical reference scan. To examine this, we repeated our main whole-brain analysis using the T₂ anatomical data in place of

the T₁. We found that using a T₂-weighted anatomical scan as a reference for alignment purposes had little effect on our results (ANOVAs, main effects of condition, $F_{6,30} > 50.4$, p -values $< 5 \times 10^{-36}$; compare results in Supplemental Figure 13 and Figure 4).

3.5 | Analysis #5: PA PE data

The pattern of geometric distortion due to B₀ inhomogeneity in EPI data depends critically on the PE direction (Figure 1) (Andersson et al., 2003; Embleton et al., 2010; Morgan et al., 2004; Mori et al., 2018). To examine whether our findings were specific to data with an AP PE direction, we repeated an earlier whole-brain analysis (#2: prealigned data) using GE EPI data with the opposite (PA) PE direction (see Section 2 for details). The results of this analysis largely recapitulated our earlier findings (ANOVAs, main effects of condition, $F_{6,30} > 26.1$, p -values $< 2 \times 10^{-22}$; compare data in Supplemental Figure 14 with those in Supplemental Figure 11), suggesting that the choice of an AP or PA PE direction did not have a dramatic effect on our results. In Supplemental Figure 15, we show an example of the subtraction between distortion-corrected AP and PA data in a single subject. This method has previously been used to quantify residual error, as a metric for distortion compensation quality (In et al., 2017).

As shown in Figure 8, across all subjects residual errors for AP–PA data are lowest in the GE oppPE conditions (ANOVA, main effect of condition, $F_{5,30} = 661, p < 9 \times 10^{-98}$), consistent with superior distortion compensation.

3.6 | Analysis #6: Young adult HCP data

To assess how well our findings would generalize outside our own dataset, we conducted another analysis using similar methods with 7 T GE EPI data from the Young Adult HCP dataset (Benson et al., 2018; Glasser et al., 2016; Van Essen et al., 2013; Vu et al., 2017). Distortion compensation using SE oppPE field maps within our processing pipeline tended to improve correspondence between EPI and T_1 data from the Young Adult HCP (compared to alignment-only data; ANOVA, main effects of condition, $F_{3,19} > 66.1$, p -values $< 2 \times 10^{-18}$; Supplemental Figure 16), and yielded similar results to those obtained using SE oppPE methods in our main analysis (compare blue symbols to those in Figure 4).

3.7 | Analysis #7: Correcting SE data

Up to this point, we have focused on distortion correction of GE EPI data at 7 T. Our results have generally shown superior performance for GE oppPE field map scans over SE oppPE methods (e.g., Figure 4),

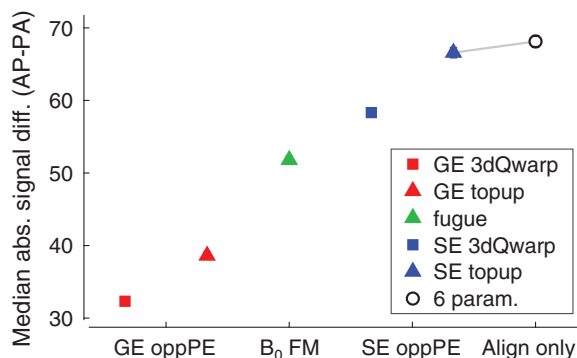


FIGURE 8 Residual error for anterior–posterior (AP) minus posterior–anterior (PA) data. Residual error was calculated by taking the difference between AP (Analysis #2: prealigned data) and PA (Analysis #5: PA PE data) echo planar imaging (EPI) data, as in Supplemental Figure 15. Gray lines indicate conditions that do not differ significantly (post hoc paired t tests, threshold $p < 0.05$, false discovery rate [FDR] corrected). X-axis labels: gradient echo (GE) oppPE = gradient echo opposite phase encoding field map (red); B₀ FM = B₀ field map (green); SE oppPE = spin echo opposite phase encoding field map (blue); Align only = alignment-only (no explicit geometric distortion compensation). Squares show data corrected using AFNI, triangles show data from FSL, and circles show alignment-only data. Symbols are the mean across subjects. Error bars (generally smaller than symbols) are SEM calculated within subjects (Morey, 2008). Data are in arbitrary (scanner) units. GE oppPE methods showed the lowest residual error (signal difference), consistent with superior distortion compensation

except in regions with severe dropout (i.e., vmPFC; Figure 6). One possibility is that GE oppPE field maps may not be superior overall, but may be better for correcting GE data in particular, whereas SE oppPE field maps may yield superior correction of SE data. Further, including the EPI scan to-be corrected as one half of the oppPE scan pair may result in superior correction. We sought to address this by applying our analyses to SE, rather than GE data. As predicted, distortion compensation quality metrics varied significantly across conditions (ANOVA, main effects of condition, $F_{4,19} > 153$, p -values $< 2 \times 10^{-35}$; Supplemental Figure 17), with SE oppPE methods outperforming GE oppPE methods when applied to SE EPI data. Alongside our other results, this suggests that matching the oppPE field map to the data type to-be corrected yields superior distortion compensation.

4 | DISCUSSION

Our analyses showed that all of the distortion compensation methods tested (GE oppPE field maps, B₀ field maps, SE oppPE field maps) yielded overall improved correspondence between GE fMRI and T_1 anatomical data across the whole brain, compared to alignment-only data. We found very few differences when comparing our results for oppPE field map corrections performed using AFNI versus FSL (squares vs. triangles, Figure 4), suggesting that these two software packages generally yield equivalent data quality for this type of distortion compensation. However, we did find small but consistent differences in Dice coefficients and mutual information between the various distortion compensation methods we examined. Agreement between GE fMRI and T_1 data across the whole brain was generally highest in our dataset when using GE oppPE field maps for distortion compensation (red symbols, Figure 4). Hence, we have chosen to implement this particular correction method within our own internal data processing pipeline for the Psychosis HCP.

Although it has been theorized that SE oppPE field maps might yield overall better distortion compensation than GE oppPE methods (Holland et al., 2010), we generally observed better distortion correction, as quantified by Dice coefficients and mutual information, for GE versus SE oppPE methods in our whole-brain analyses of GE data (e.g., red vs. blue symbols, Figure 4). However, Analysis #7 (correcting SE data) showed that SE oppPE methods did outperform GE oppPE field maps when applied to correct SE EPI data in particular. Thus, we conclude that matching the type of oppPE field map to the EPI data to-be corrected (whether GE or SE), and including the EPI data of interest as one half of the oppPE pair, yields better distortion compensation than correcting one type of data with the other type of oppPE field map data. We offer two plausible explanations for this finding below.

A similar overall pattern to our whole-brain results (Figure 4) was observed within dmPFC (Figure 7), a region with significant geometric distortion, but not in vmPFC (Figure 6), where both significant distortion and substantial signal dropout due to through-slice dephasing are observed. In vmPFC, we saw somewhat better performance

(higher Dice coefficients; Figure 6a,b) for SE versus GE oppPE methods, consistent with the notion that SE oppPE field maps would yield better distortion compensation due to reduced through-slice dephasing (Holland et al., 2010). However, Dice coefficients for the SE oppPE methods were generally not higher than for the alignment-only conditions, and we saw no differences in mutual information between T_1 and EPI data within vmPFC across conditions (Figure 6c). In contrast, the patterns of results in the dmPFC ROI (Figure 7) were similar to those from the whole-brain analyses (Figure 4). Together, these results suggest that for GE EPI data, the advantages (if any) of the SE oppPE approach were limited to regions of the brain with strong drop-out (such as vmPFC), whereas the GE oppPE approach tended to produce better results in our GE data overall.

This study provides a framework for deciding which distortion compensation method to use for a given dataset, based on quantitative comparisons of the agreement between distortion-corrected EPI data and an anatomical reference scan. We expect that the relative performance of different methods may vary across datasets based on data acquisition parameters, scanner and coil hardware, and the details of the processing pipelines that are used. Thus, the reader may wish to compare the relative performance of different distortion compensation methods in their own dataset using an approach similar to ours. We used multiple metrics to quantify EPI- T_1 agreement as a proxy for correction quality (i.e., Dice coefficients for whole-brain masks and CSF-excluded masks, as well as mutual information), since we acknowledge that there is no single gold standard for measuring the quality of distortion compensation in human brain imaging data (Hong et al., 2015) (but see the following studies that used simulations to try to establish ground truth (Esteban et al., 2014; Graham et al., 2017)). Across our analyses, we found that certain methodological decisions (i.e., whether or not to align data prior to distortion compensation, the use of single-band reference, T_2 anatomical, or PA GE data) had little effect on our pattern of results (compare Figure 4 with Supplemental Figures 11–14), whereas regional variations in distortion compensation metrics were more dramatic (Figures 6 and 7; Supplemental Figure 10). We found results comparable to our main findings when examining data from the Young Adult HCP study (Supplemental Figure 16). By making our data and analysis code publicly available (see Section 2), we hope to facilitate the empirical selection of effective approaches for geometric distortion compensation in future research.

In addition to geometric distortion compensation, our analyses included gradient nonlinearity correction (Bakker et al., 1992; Glasser et al., 2013; Jezzard & Clare, 1999), a postprocessing step to correct for static spatial nonuniformities in the brain images caused by the gradients themselves (i.e., not dependent on the scanning sequence or B_0 field inhomogeneity). In our data, we found gradient nonlinearities led to voxel shifts up to about 4 mm in some regions (Supplemental Figure 1; Supplemental Table 1). Correcting for this type of image distortion is particularly important in cases such as ours, where one wishes to align EPI and anatomical data acquired in different scanning sessions, as distortions due to gradient nonlinearities will vary across scanners based on differences in gradient hardware, and across

scanning sessions based on head position. Previous studies comparing different geometric distortion compensation methods have generally not included (or reported) gradient nonlinearity correction. For datasets acquired in a single scanning session, sequence-independent gradient nonlinearities limit geometric fidelity but not the ability to align distortion corrected EPI to anatomical reference scans. We believe that effective corrections for both gradient nonlinearities and geometric distortions are critical for achieving high spatial fidelity, and for harmonizing EPI and T_1 data across different scanning sessions or field strengths.

We did not initially hypothesize that GE oppPE methods would outperform SE methods in our GE data, but rather sought to explore which method would perform best in our dataset. We offer two possible explanations for this finding, which are not mutually exclusive. First, there may be more opportunities for head motion to degrade the quality of distortion compensation when using a SE oppPE field map to correct GE EPI data (or vice-versa), as there are two additional scans (forward and reverse PE SE) during and between which the subject must hold still, versus only one additional scan for a GE oppPE field map (reverse GE, as the GE EPI data to-be corrected may serve as the forward PE half of the GE oppPE pair). As noted below, any head motion between scans will change the B_0 inhomogeneities and subsequent geometric distortions, leading to poorer correction. Including the EPI scan to-be corrected as half of the oppPE pair may also allow the unwarping algorithm to correct any geometric differences between scans due to head motion, in addition to those caused by B_0 inhomogeneity distortion. We examined the effect of motion in a series of post hoc analyses (see Supplemental methods), in which we correlated our distortion compensation metrics against residual head motion between our GE EPI data (following distortion compensation) and our different field map scans. The data shown in Supplemental Figures 18 and 19 suggest that greater head motion between SE field map and GE EPI scans may have contributed to poorer distortion compensation for the SE oppPE methods (vs. GE oppPE), but that this may not fully account for the overall reduced performance we observed for SE corrections. Future studies that acquire multiple SE oppPE field map scans at different time points, or in which subjects are explicitly instructed to move their heads between scans, may be better able to directly examine this possibility.

Second, superior performance of the GE oppPE field maps for correcting GE data might possibly be attributed to differences in image contrast between GE and SE data (Embleton et al., 2010; Graham et al., 2017) (compare Figure 1a,b vs. Figure 1g,h). In regions of significant B_0 inhomogeneity, geometric distortion can cause displaced signal from multiple voxels to 'pile up' within a single voxel (i.e., local compression) (Andersson et al., 2003; Li et al., 2006; Li et al., 2007; Wan et al., 1997). Local compression depends on PE direction; oppPE field map methods attempt to correct for compression by using interpolation to recreate the image 'in between' the forward and reverse PE scans. If local compression differs between SE and GE scans, as would be expected due to contrast differences, then the mapping of spatial information during oppPE distortion compensation may also differ. In this case, the warp field calculated from SE

oppPE field maps (and applied to GE EPI data; or vice versa) may be incorrect in regions of local compression, resulting in poorer distortion compensation (Embleton et al., 2010; Graham et al., 2017). This issue of signal compression during distortion compensation has also been appreciated in the dMRI field; local compression differs for scans with different diffusion weighting (and thus different signal contrast), which is relevant for distortion compensation of such data using oppPE methods (Embleton et al., 2010; Graham et al., 2017).

Our results agree with previous studies that have universally shown corrections for geometric distortion due to B_0 field inhomogeneity improve EPI data quality and alignment with minimally distorted reference scans (Hutton et al., 2002). In particular, previous work has generally shown better performance for oppPE field map strategies, as compared to B_0 field maps, which has been attributed in part to the difficulty of using B_0 field maps to correct distortion near the edges of the brain (see Figure 1f), where phase values change rapidly across space. Using simulated EPI data, both Esteban (Esteban et al., 2014) and Graham (Graham et al., 2017) showed quantitatively that ground truth undistorted images were recovered best using an oppPE field map method, whereas B_0 field maps performed slightly worse, and nonlinear registration-based methods were greatly inferior (but still better than no correction at all). Similar conclusions were reached by Hong et al. (2015) using SE EPI in the mouse brain at 7 T, by Holland et al. (2010) using SE EPI at 1.5 and 3 T in the human brain, and by Wang et al. (2017) using 3 T dMRI data in humans (see also Gholipour et al., 2011). Thus, there is some evidence to suggest, in general terms, better performance for oppPE methods over B_0 field maps, with nonlinear registration yielding poorer results (but better than no correction, and useful in cases where the additional scans required to perform the other methods above are not available).

This study considered only static geometric distortions in the GE EPI data caused by B_0 inhomogeneity. If a subject moves during a scanning session, then the B_0 inhomogeneities will not be stable over time, and geometric distortions will vary with head motion (Hutton et al., 2002), resulting in poorer correction based on static methods (Graham et al., 2017). We conducted a series of analyses to examine the impact of head motion on our results (Supplemental Figures 11, 18, and 19). Our findings suggest that greater head motion was associated with somewhat lower Dice coefficient values, but that differences across field map methods in subject head motion over time may not fully account for the pattern of results we observed. Methods for dynamic distortion compensation (e.g., with different distortion fields calculated for each time point in an EPI time series) have also been proposed (Andersson et al., 2001; Barry et al., 2010; Dymerska et al., 2018), and may offer advantages in correcting time-varying geometric distortion, as compared to the static approaches considered here. However, to our knowledge, such dynamic distortion compensation methods are not currently implemented in the software packages that are most often used to preprocess brain imaging data.

ACKNOWLEDGMENTS

The authors thank Jesslyn (Li Shen) Chong, Tori Espensen-Sturges, Andrea N. Grant, Rohit S. Kamath, Timothy J. Lano, and Marisa

J. Sanchez for their assistance with data collection. The authors also thank Bryon A. Mueller and Hannah R. Moser for help with data processing, and Essa Yacoub for supporting the design of the study. This work was supported by funding from the National Institutes of Health (U01 MH108150). Salary support for M.-P. S. was provided by K01 MH120278. Salary support for C. A. O. was provided by R01 MH111447. Support for MR scanning at the University of Minnesota Center for Magnetic Resonance Research was provided by P41 EB015894 and P30 NS076408. This work used tools from the University of Minnesota Clinical and Translational Science Institute that were supported by UL1 TR002494. The authors declare that they have no conflicts of interest with regard to the publication of this manuscript.

DATA AVAILABILITY STATEMENT

Our analysis code is available on GitHub (github.com/mpschallmo/DistortionCompensation). Imaging data are available from the Human Connectome Project (intradb.humanconnectome.org; first Psychosis Human Connectome Project data release planned for 3rd quarter, 2021).

ORCID

Michael-Paul Schallmo  <https://orcid.org/0000-0001-8252-8607>

Kimberly B. Weldon  <https://orcid.org/0000-0003-4349-9916>

Cheryl A. Olman  <https://orcid.org/0000-0002-7324-6461>

REFERENCES

- Andersson, J. L. R., Hutton, C., Ashburner, J., Turner, R., & Friston, K. (2001a). Modeling geometric deformations in EPI time series. *NeuroImage*, 13(5), 903–919. <https://doi.org/10.1006/nimg.2001.0746>
- Andersson, J. L. R., Skare, S., & Ashburner, J. (2003a). How to correct susceptibility distortions in spin-echo echo-planar images: application to diffusion tensor imaging. *NeuroImage*, 20(2), 870–888. [https://doi.org/10.1016/S1053-8119\(03\)00336-7](https://doi.org/10.1016/S1053-8119(03)00336-7)
- Bakker, C. J. G., Moerland, M. A., Bhawandien, R., & Beersma, R. (1992a). Analysis of machine-dependent and object-induced geometric distortion in 2DFT MR imaging. *Magnetic resonance imaging*, 10(4), 597–608. [https://doi.org/10.1016/0730-725X\(92\)90011-N](https://doi.org/10.1016/0730-725X(92)90011-N)
- Barry, R. L., Williams, J. M., Klassen, L. M., Gallivan, J. P., Culham, J. C., & Menon, R. S. (2010a). Evaluation of preprocessing steps to compensate for magnetic field distortions due to body movements in BOLD fMRI. *Magnetic resonance imaging*, 28(2), 235–244. <https://doi.org/10.1016/j.mri.2009.07.005>
- Benson, N. C., Jamison, K. W., Arcaro, M. J., Vu, A. T., Glasser, M. F., Coalson, T. S., ... Kay, K. (2018a). The Human Connectome Project 7 Tesla retinotopy dataset: Description and population receptive field analysis. *Journal of Vision*, 18(13), 23.
- Cox, R. W. (1996a). AFNI: software for analysis and visualization of functional magnetic resonance neuroimages. *Computers and Biomedical research*, 29(3), 162–173.
- Dale, A. M., Fischl, B., & Sereno, M. I. (1999a). Cortical surface-based analysis. I. Segmentation and surface reconstruction. *NeuroImage*, 9, 179–194.
- Dale, A. M., & Sereno, M. I. (1993a). Improved localization of cortical activity by combining EEG and MEG with MRI cortical surface reconstruction: A linear approach. *Journal of Cognitive Neuroscience*, 5(2), 162–176.
- Dymerska, B., Poser, B. A., Barth, M., Tractnig, S., & Robinson, S. D. (2018a). A method for the dynamic correction of B_0 -related

- distortions in single-echo EPI at 7 T. *NeuroImage*, 168, 321–331. <https://doi.org/10.1016/j.neuroimage.2016.07.009>
- Embleton, K. V., Haroon, H. A., Morris, D. M., Ralph, M. A. L., & Parker, G. J. M. (2010a). Distortion correction for diffusion-weighted MRI tractography and fMRI in the temporal lobes. *Human Brain Mapping*, 31(10), 1570–1587. <https://doi.org/10.1002/hbm.20959>
- Esteban, O., Daducci, A., Caruyer, E., O'Brien, K., Ledesma-Carbayo, M. J., Bach-Cuadra, M., & Santos, A. (2014a, 4/2014). *Simulation-based evaluation of susceptibility distortion correction methods in diffusion MRI for connectivity analysis*. Paper presented at the 2014 IEEE 11th International Symposium on Biomedical Imaging (ISBI 2014).
- Feinberg, D. A., & Oshio, K. (1994a). Phase errors in multi-shot echo planar imaging. *Magnetic Resonance in Medicine*, 32(4), 535–539. <https://doi.org/10.1002/mrm.1910320418>
- Friston, K. J., Holmes, A. P., Worsley, K. J., Poline, J.-P., Frith, C. D., & Frackowiak, R. S. J. (1994a). Statistical parametric maps in functional imaging: A general linear approach. *Human Brain Mapping*, 2, 189–210. <https://doi.org/10.1002/hbm.460020402>
- Gholipour, A., Kehtarnavaz, N., Scherrer, B., & Warfield, S. K. (2011). On the accuracy of unwarping techniques for the correction of susceptibility-induced geometric distortion in magnetic resonance Echo-planar images. In *2011 33rd Annual International Conference of the IEEE Engineering in Medicine and Biology Society*. 6997–7000.
- Gholipour, A., Kehtarnavaz, N., Gopinath, K., Briggs, R., Devous, M., & Haley, R. (2006a, 10/2006). *Distortion correction via non-rigid registration of functional to anatomical magnetic resonance brain images*. Paper presented at the 2006 International Conference on Image Processing.
- Gholipour, A., Kehtarnavaz, N., Scherrer, B., & Warfield, S. K. (2011a, 08/2011). *On the accuracy of unwarping techniques for the correction of susceptibility-induced geometric distortion in magnetic resonance Echo-planar images*. Paper presented at the 2011 33rd Annual International Conference of the IEEE Engineering in Medicine and Biology Society.
- Glasser, M. F., Smith, S. M., Marcus, D. S., Andersson, J. L. R., Auerbach, E. J., Behrens, T. E. J., ... Van Essen, D. C. (2016a). The Human Connectome Project's neuroimaging approach. *Nature neuroscience*, 19(9), 1175–1187. <https://doi.org/10.1038/nn.4361>
- Glasser, M. F., Sotiropoulos, S. N., Wilson, J. A., Coalson, T. S., Fischl, B., Andersson, J. L., ... Jenkinson, M. (2013a). The minimal preprocessing pipelines for the Human Connectome Project. *NeuroImage*, 80, 105–124. <https://doi.org/10.1016/j.neuroimage.2013.04.127>
- Glover, G. H., & Law, C. S. (2001a). Spiral-in/out BOLD fMRI for increased SNR and reduced susceptibility artifacts. *Magnetic Resonance in Medicine*, 46(3), 515–522. <https://doi.org/10.1002/mrm.1222>
- Andersson, J. L. R., Hutton, C., Ashburner, J., Turner, R., & Friston, K. (2001b). Modeling geometric deformations in EPI time series. *NeuroImage*, 13(5), 903–919. <https://doi.org/10.1006/nimg.2001.0746>
- Andersson, J. L. R., Skare, S., & Ashburner, J. (2003b). How to correct susceptibility distortions in spin-echo echo-planar images: application to diffusion tensor imaging. *NeuroImage*, 20(2), 870–888. [https://doi.org/10.1016/S1053-8119\(03\)00336-7](https://doi.org/10.1016/S1053-8119(03)00336-7)
- Bakker, C. J. G., Moerland, M. A., Bhwandien, R., & Beersma, R. (1992b). Analysis of machine-dependent and object-induced geometric distortion in 2DFT MR imaging. *Magnetic resonance imaging*, 10(4), 597–608. [https://doi.org/10.1016/0730-725X\(92\)90011-N](https://doi.org/10.1016/0730-725X(92)90011-N)
- Barry, R. L., Williams, J. M., Klassen, L. M., Gallivan, J. P., Culham, J. C., & Menon, R. S. (2010b). Evaluation of preprocessing steps to compensate for magnetic field distortions due to body movements in BOLD fMRI. *Magnetic resonance imaging*, 28(2), 235–244. <https://doi.org/10.1016/j.mri.2009.07.005>
- Benson, N. C., Jamison, K. W., Arcaro, M. J., Vu, A. T., Glasser, M. F., Coalson, T. S., ... Kay, K. (2018b). The Human Connectome Project 7 Tesla retinotopy dataset: Description and population receptive field analysis. *Journal of Vision*, 18(13), 23.
- Cox, R. W. (1996b). AFNI: software for analysis and visualization of functional magnetic resonance neuroimages. *Computers and Biomedical research*, 29(3), 162–173.
- Dale, A. M., Fischl, B., & Sereno, M. I. (1999b). Cortical surface-based analysis. I. Segmentation and surface reconstruction. *NeuroImage*, 9, 179–194.
- Dale, A. M., & Sereno, M. I. (1993b). Improved localization of cortical activity by combining EEG and MEG with MRI cortical surface reconstruction: A linear approach. *Journal of Cognitive Neuroscience*, 5(2), 162–176.
- Dymerska, B., Poser, B. A., Barth, M., Trattnig, S., & Robinson, S. D. (2018b). A method for the dynamic correction of B0-related distortions in single-echo EPI at 7 T. *NeuroImage*, 168, 321–331. <https://doi.org/10.1016/j.neuroimage.2016.07.009>
- Embleton, K. V., Haroon, H. A., Morris, D. M., Ralph, M. A. L., & Parker, G. J. M. (2010b). Distortion correction for diffusion-weighted MRI tractography and fMRI in the temporal lobes. *Human Brain Mapping*, 31(10), 1570–1587. <https://doi.org/10.1002/hbm.20959>
- Esteban, O., Daducci, A., Caruyer, E., O'Brien, K., Ledesma-Carbayo, M. J., Bach-Cuadra, M., & Santos, A. (2014b, 4/2014). *Simulation-based evaluation of susceptibility distortion correction methods in diffusion MRI for connectivity analysis*. Paper presented at the 2014 IEEE 11th International Symposium on Biomedical Imaging (ISBI 2014).
- Feinberg, D. A., & Oshio, K. (1994b). Phase errors in multi-shot echo planar imaging. *Magnetic Resonance in Medicine*, 32(4), 535–539. <https://doi.org/10.1002/mrm.1910320418>
- Friston, K. J., Holmes, A. P., Worsley, K. J., Poline, J.-P., Frith, C. D., & Frackowiak, R. S. J. (1994b). Statistical parametric maps in functional imaging: A general linear approach. *Human Brain Mapping*, 2, 189–210. <https://doi.org/10.1002/hbm.460020402>
- Gholipour, A., Kehtarnavaz, N., Gopinath, K., Briggs, R., Devous, M., & Haley, R. (2006b, 10/2006). *Distortion correction via non-rigid registration of functional to anatomical magnetic resonance brain images*. Paper presented at the 2006 International Conference on Image Processing.
- Gholipour, A., Kehtarnavaz, N., Scherrer, B., & Warfield, S. K. (2011b, 08/2011). *On the accuracy of unwarping techniques for the correction of susceptibility-induced geometric distortion in magnetic resonance Echo-planar images*. Paper presented at the 2011 33rd Annual International Conference of the IEEE Engineering in Medicine and Biology Society.
- Glasser, M. F., Smith, S. M., Marcus, D. S., Andersson, J. L. R., Auerbach, E. J., Behrens, T. E. J., ... Van Essen, D. C. (2016b). The Human Connectome Project's neuroimaging approach. *Nature neuroscience*, 19(9), 1175–1187. <https://doi.org/10.1038/nn.4361>
- Glasser, M. F., Sotiropoulos, S. N., Wilson, J. A., Coalson, T. S., Fischl, B., Andersson, J. L., ... Jenkinson, M. (2013b). The minimal preprocessing pipelines for the Human Connectome Project. *NeuroImage*, 80, 105–124. <https://doi.org/10.1016/j.neuroimage.2013.04.127>
- Glover, G. H., & Law, C. S. (2001b). Spiral-in/out BOLD fMRI for increased SNR and reduced susceptibility artifacts. *Magnetic Resonance in Medicine*, 46(3), 515–522. <https://doi.org/10.1002/mrm.1222>
- Olman, C. A., & Yacoub, E. (2011). High-field fMRI for human applications: An overview of spatial resolution and signal specificity. *The Open Neuroimaging Journal*, 5, 74–89.
- Robson, M. D., Gore, J. C., & Constable, R. T. (1997). Measurement of the point spread function in MRI using constant time imaging. *Magnetic Resonance in Medicine*, 38(5), 733–740. <https://doi.org/10.1002/mrm.1910380509>
- Saad, Z. S., Glen, D. R., Chen, G., Beauchamp, M. S., Desai, R., & Cox, R. W. (2009). A new method for improving functional-to-structural MRI alignment using local Pearson correlation. *NeuroImage*, 44, 839–848.
- Smith, S. M., Jenkinson, M., Woolrich, M. W., Beckmann, C. F., Behrens, T. E. J., Johansen-Berg, H., ... Matthews, P. M. (2004). Advances in functional and structural MR image analysis and implementation as FSL. *NeuroImage*, 23(S1), 208–219.

- Studholme, C., Constable, R. T., & Duncan, J. S. (2000). Accurate alignment of functional EPI data to anatomical MRI using a physics-based distortion model. *IEEE Transactions on Medical Imaging*, 19(11), 1115–1127. <https://doi.org/10.1109/42.896788>
- Studholme, C., Hill, D. L. G., & Hawkes, D. J. (1999). An overlap invariant entropy measure of 3D medical image alignment. *Pattern Recognition*, 32(1), 71–86. [https://doi.org/10.1016/S0031-3203\(98\)00091-0](https://doi.org/10.1016/S0031-3203(98)00091-0)
- Sumanaweera, T. S., Adler, J. R., Glover, G. H., Hemler, P. F., van den Elsen, P. A., Martin, D., & Napel, S. (1995). Method for correcting magnetic resonance image distortion for frame-based stereotactic surgery, with preliminary results. *Journal of Image Guided Surgery*, 1(3), 151–157.
- Sumanaweera, T. S., Glover, G. H., Binford, T. O., & Adler, J. R. (1993). MR susceptibility misregistration correction. *IEEE Transactions on Medical Imaging*, 12(2), 251–259.
- T. Vu, A., Jamison, K., Glasser, M. F., Smith, S. M., Coalson, T., Moeller, S., ... Yacoub, E. (2017). Tradeoffs in pushing the spatial resolution of fMRI for the 7T Human Connectome Project. *NeuroImage*, 154, 23–32. doi:<https://doi.org/10.1016/j.neuroimage.2016.11.049>
- Van Essen, D. C., Smith, S. M., Barch, D. M., Behrens, T. E. J., Yacoub, E., & Ugurbil, K. (2013). The WU-Minn Human Connectome Project: An overview. *NeuroImage*, 80(15), 62–79.
- Vu, A. T., Auerbach, E., Lenglet, C., Moeller, S., Sotiropoulos, S. N., Jbabdi, S., ... Ugurbil, K. (2015). High resolution whole brain diffusion imaging at 7 T for the Human Connectome Project. *NeuroImage*, 122, 318–331. <https://doi.org/10.1016/j.neuroimage.2015.08.004>
- Wan, X., Gullberg, G. T., Parker, D. L., & Zeng, G. L. (1997). Reduction of geometric and intensity distortions in echo-planar imaging using a multireference scan. *Magnetic Resonance in Medicine*, 37(6), 932–942. <https://doi.org/10.1002/mrm.1910370619>
- Wang, S., Peterson, D. J., Gatenby, J. C., Li, W., Grabowski, T. J., & Madhyastha, T. M. (2017). Evaluation of field map and nonlinear registration methods for correction of susceptibility artifacts in diffusion MRI. *Frontiers in Neuroinformatics*, 11, 1–9. <https://doi.org/10.3389/fninf.2017.00017>
- Zaitsev, M., Hennig, J., & Speck, O. (2004). Point spread function mapping with parallel imaging techniques and high acceleration factors: Fast, robust, and flexible method for echo-planar imaging distortion correction. *Magnetic Resonance in Medicine*, 52(5), 1156–1166. <https://doi.org/10.1002/mrm.20261>
- Zeng, H., & Constable, R. T. (2002). Image distortion correction in EPI: Comparison of field mapping with point spread function mapping. *Magnetic Resonance in Medicine*, 48(1), 137–146. <https://doi.org/10.1002/mrm.10200>

SUPPORTING INFORMATION

Additional supporting information may be found online in the Supporting Information section at the end of this article.

How to cite this article: Schallmo, M.-P., Weldon, K. B., Burton, P. C., Sponheim, S. R., & Olman, C. A. (2021). Assessing methods for geometric distortion compensation in 7 T gradient echo functional MRI data. *Human Brain Mapping*, 42(13), 4205–4223. <https://doi.org/10.1002/hbm.25540>